mathematics

MDPI

Article

An Adaptive Inertia and Damping Control Strategy Based on Enhanced Virtual Synchronous Generator Model

Aleksey Suvorov [1,*], Alisher Askarov [1], Nikolay Ruban [1], Vladimir Rudnik [1], Pavel Radko [1], Andrey Achitaev [2] and Konstantin Suslov [3]

[1] School of Energy & Power Engineering, National Research Tomsk Polytechnic University, Tomsk 634050, Russia; aba7@tpu.ru (A.A.); rubanny@tpu.ru (N.R.); ver3@tpu.ru (V.R.); ppr1@tpu.ru (P.R.)
[2] Department of Hydropower, Hydroelectric Power Plants, Electricity Systems and Electricity Networks, Siberian Federal University, Krasnoyarsk 660041, Russia; aachitaev@shf-sfu.ru
[3] Department of Power Supply and Electrical Engineering, Irkutsk National Research Technical University, Irkutsk 664074, Russia; suslovkv@mpei.ru
* Correspondence: suvorovaa@tpu.ru

Abstract: In modern converter-dominated power systems, total inertia is very variable and depends on the share of power generated by renewable-based converter-interfaced generation (CIG) at each specific moment. As a result, the limits required by the grid codes on the rate of change of frequency and its nadir or zenith during disturbances become challenging to achieve with conventional control approaches. Therefore, the transition to a novel control strategy of CIG with a grid-forming power converter is relevant. For this purpose, a control algorithm based on a virtual synchronous generator (VSG) is used, which simulates the properties and capabilities of a conventional synchronous generation. However, due to continuously changing operating conditions in converter-dominated power systems, the virtual inertia formed by VSG must be adaptive. At the same time, the efficiency of adaptive algorithms strongly depends on the used VSG structure. In this connection, this paper proposes an enhanced VSG structure for which the transfer function of the active power control loop was formed. With the help of it, the advantages over the conventional VSG structure were proven, which are necessary for the effective adaptive control of the VSG parameters. Then, the analysis of the impact of the VSG parameters on the dynamic response using the transient characteristics in the time domain was performed. Based on the results obtained, adaptive algorithms for independent control of the virtual inertia and the parameters of the VSG damper winding were developed. The performed mathematical modeling confirmed the reliable and effective operation of the developed adaptive control algorithms and the enhanced VSG structure. The theoretical and experimental results obtained in this paper indicate the need for simultaneous development and improvement of both adaptive control algorithms and VSG structures used for this purpose.

Keywords: virtual synchronous generator; power converter; adaptive control; grid-forming; virtual inertia; frequency response

MSC: 93D21; 93C40; 03C85

Citation: Suvorov, A.; Askarov, A.; Ruban, N.; Rudnik, V.; Radko, P.; Achitaev, A.; Suslov, K. An Adaptive Inertia and Damping Control Strategy Based on Enhanced Virtual Synchronous Generator Model. *Mathematics* **2023**, *11*, 3938. https://doi.org/10.3390/math11183938

Academic Editor: Svetlana V. Solodusha

Received: 18 August 2023
Revised: 12 September 2023
Accepted: 14 September 2023
Published: 16 September 2023

1. Introduction

With the development of distributed generation units based on renewable energy sources, the number of power converters in modern power systems is significantly increasing, leading to trends in the transformation of power systems into converter-dominated power systems. One of the main problems of such power systems is the inconstancy of inertia, the value of which depends on the share of power generated by renewable-based converter-interfaced generation (CIG) at each specific moment [1]. It is well known that inertia plays a major role in the formation of the grid frequency response during the first seconds of the transients under small or large disturbances in power systems [2,3]. The

value of inertia determines the rate of change of frequency (RoCoF) and the value of its nadir or zenith, the maximum permissible values of which are strictly regulated in the grid codes of various countries [4]. The importance of the latter is associated with the provision of reliable operation of automation devices and stability of power systems, which becomes very challenging under the development of converter-dominated power systems and requires the use of novel smart and flexible technologies [5,6].

A unique feature of power converters is the dynamics of their operation, which is determined by high-speed power semiconductor switches and the corresponding high-speed control system, which together provide wide opportunities for using converters to solve a wide range of tasks [7,8]. In this regard, the transition from the conventional grid-following control of power converters to the novel control strategy with so-called grid-forming power converters is particularly relevant [9,10]. Such a solution allows the provision of the necessary inertial response with CIG, which is determinative at the primary frequency regulation [11,12]. The most promising direction is the control based on the virtual synchronous generator (VSG), which allows to mimic the behavior of a conventional synchronous generator [13]. However, the efficiency of VSG performance significantly depends on the set parameters [14]. At the same time, due to continuously changing operating conditions in modern power systems, the selection of fixed parameters or rigid VSG structures does not allow the achievement of the desired control objectives. There is always a need to find a trade-off between reliability and efficiency of regulation, e.g., during changes in grid strength [15]. Thus, given the continuously changing total inertia in modern power systems, the virtual inertia formed by VSG must be adaptive to changing grid conditions to provide permissible ranges in RoCoF and magnitude of frequency deviation [16,17].

Various approaches to the development of adaptive virtual inertia algorithms are proposed as VSG enhancements. This becomes possible due to the lack of dependence of the VSG on the parameters of a real synchronous machine. One of the first solutions in this area is the VSG-based control system with an alternative moment of inertia, where the virtual inertia in the swing equation was modified using bang–bang control [18]. Such an approach made it possible not only to improve the oscillations damping but also to increase the power system stability. At the same time, in the case of frequency deviation, the virtual inertia changes only to the maximum or minimum value. In order to reduce the number of excessive control actions, it is proposed to use an additional value of virtual inertia with bang–bang control, and recommendations on the tuning are given [19]. A modified hybrid algorithm for adaptive control of virtual inertia using bang–bang control has also been developed [20]. It is worth noting that algorithms based on such a principle are quite simple to implement. However, they always use the maximum available energy due to the discontinuously changing value of inertia, which can lead to unwanted oscillations of parameters in the steady-state. In order to exclude this feature, the deadband controllers are inevitably added to the control system. As a consequence, a delay emerges during the algorithm operation, which directly depends on the deadband range [21].

The predominant direction for improving the adaptive control of the VSG inertia is an additional real-time change of the damping coefficient [22]. The coordinated control of the virtual inertia and the damping coefficient ensures the highest efficiency of oscillation suppression [23] and improves the frequency regulation of the parallel CIGs [24]. Basically, all approaches for co-adaptive control of the two indicated parameters are based on determining the optimal damping ratio [25,26]. Taking into account the shortcomings of the bang–bang control, other approaches to adaptive virtual inertia are also proposed. In Ref. [27], it is proposed to change VSG inertia according to a nonlinear function formulated only based on the deviation of the angular frequency of the virtual rotor. To reduce the impact of adaptive inertia on the VSG response during changes of the active power reference, the control algorithm using a nonlinear function and an adaptive priority setter is proposed [28]. It is also proposed to use the active power deviation instead of frequency control for adaptive inertia [29].

Despite the improvement of adaptive control algorithms, their efficiency largely depends on the used VSG structure. At present, most of the algorithms are designed for the power converter control systems based on the conventional voltage-controlled VSG structure (VC-VSG) [30,31]. The change of the inertia constant and the damping coefficient for such a structure inevitably leads to three fundamental contradictions [32,33]. The first of them is related to the impact of the oscillation damping efficiency on the speed of the active power response. As a result, the increase in the damping coefficient increases the rise and fall times of the CIG output power. The second is related to the impact of the damping coefficient on the frequency droop, which leads to the steady-state value of the output active power, which is different from the reference value, after the disturbance. The third contradiction arises between the response speed to the change in active power and the frequency deviation. For an appropriate active power response, it is necessary to decrease the damping coefficient, and, on the contrary, to increase the latter for an effective response to frequency deviations. Thus, taking into account the above challenges, the development of adaptive control algorithms should be accompanied by the development of the most appropriate VSG structures for them. This paper attempts to resolve the aforementioned issues in the current state of the art in adaptive control of VSG. The main contributions of this paper can be summarized as follows:

1. An alternative current-controlled VSG structure (CC-VSG), which avoids the issues inherent in the conventional VC-VSG structure, is proposed. The transfer function of the active power control loop is developed for the considered CC-VSG, with the help of which it is proven that there are no contradictions given earlier.
2. Due to the properties of the proposed CC-VSG structure, an adaptive control algorithm is developed that independently changes the three main parameters of the VSG, which affect the inertial response and damping.
3. For the adaptive virtual inertia control of the CC-VSG, an algorithm based on nonlinear sigmoid function is developed. Due to this, it became possible to flexibly control the inertia value by exceeding the RoCoF setting throughout the transients. In addition, the DC-side energy consumption during low frequency deviations is reduced without negative impact on the transient performance. Such control possibilities are difficult to implement in case of conventional algorithms based on the bang–bang control.
4. For the adaptive control of virtual damper winding of the CC-VSG, the damper winding virtual current is used as a controlled signal. This solution allows to improve the damping properties of the CC-VSG and, at the same time, excludes the impact on the swing equation, the active power response, as well as the frequency droop.

This paper is organized as follows. Section 2 provides a comparative analysis of the conventional and proposed enhanced VSG structures, as well as the results of theoretical studies proving the advantages of the proposed structure. Section 3 considers the impact of VSG parameters on the dynamic response. Based on the obtained transient characteristics in the time domain, the adaptive control algorithms are developed. Section 4 describes the approaches to the implementation of the developed adaptive control algorithms and outlines their properties and capabilities. Section 5 presents the results of time-domain simulation for the equivalent power system with CIG, proving the properties and capabilities of both the CC-VSG structure and the adaptive control algorithms proposed in this paper. Finally, in Section 6, the conclusions are drawn.

2. Comparative Analysis of Conventional and Enhanced VSG Models

The general view of the studied electrical network with the VSG-based power converter control system and its simplified representation are shown in Figure 1. The network contains a grid-connected CIG with an *LC*-filter with parameters L_f and C_f. An ideal capacitor of infinite capacity C_{DC} is used as the primary energy source. To reduce the complexity of the equations, only the inductive component L_g of the aggregated grid impedance between the power converter and the external grid is considered ($R_g = 0$). The external grid is

represented as an ideal AC voltage source with U_g, which determines the grid frequency ω_g. The parameters of the test scheme are given in Appendix A.

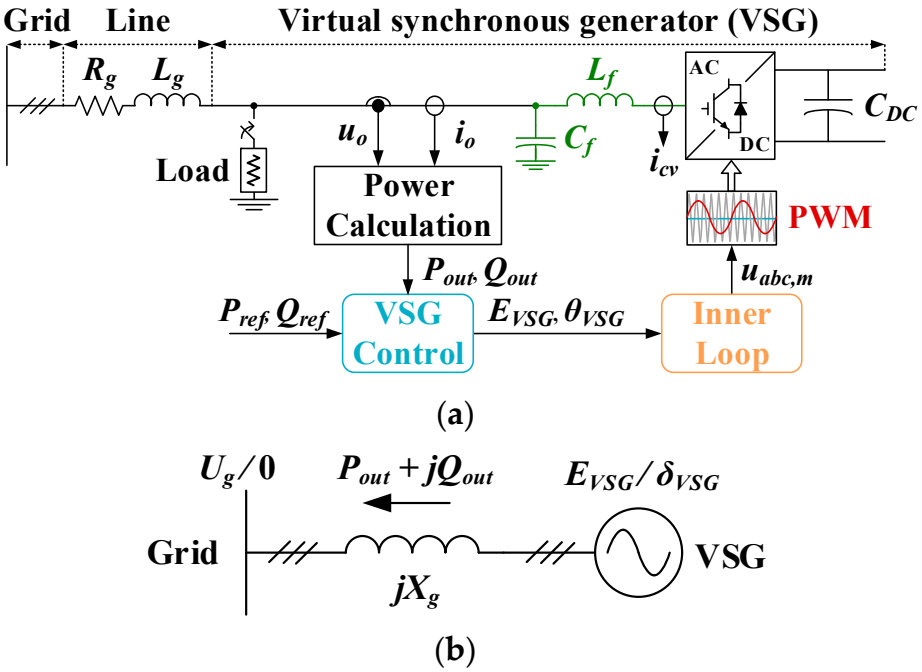

Figure 1. Test electrical network: (**a**) general diagram and control system structure; (**b**) simplified representation.

In the control system, the parameters P_{ref} and Q_{ref} are the active and reactive power references, P_{out} and Q_{out} are the output active and reactive power, i_{cv} is the converter output current, u_o and i_o are the voltage and current at the point of common coupling behind an *LC*-filter, E_{VSG} and θ_{VSG} are the magnitude and phase of the VSG output voltage, and δ_{VSG} is the angle between the voltage phase of the VSG and the external grid. The regulation of the output active and reactive power is provided by controlling the phase and magnitude of the VSG output voltage, respectively. The inner control loop is a typical part of the control system and consists of double proportional-integral controllers, which form the reference signal $u_{abc,m}$ for pulse-width modulation (PWM) with the switching frequency f_{sw}.

2.1. Conventional VC-VSG Model

Based on the main idea of the VSG-based control system, which lies in the imitation of properties and capabilities of synchronous generation, three main control loops can be identified: (i) inner control loop, (ii) model of a virtual synchronous generator, and (iii) outer control loop [14]. It is known that the VSG inertial response is determined by the swing equation of the virtual rotor used in the control structure. At the same time, by introducing a damping coefficient D, an approximate consideration of the damping properties of the synchronous generator is performed. In the conventional implementation of the VC-VSG, the damping coefficient and the droop coefficient are quite often combined, and the swing equation is transformed to the form (1):

$$\begin{cases} P_{ref} - P_{out} - D\left(\omega_{VSG} - \omega_{ref}\right) = 2H_{VSG}\frac{d\omega_{VSG}}{dt} \\ \frac{d\theta_{VSG}}{dt} = \omega_{VSG}\omega_b \end{cases} \quad (1)$$

where ω_{VSG} is the actual VSG angular frequency, pu; H_{VSG} is the VSG inertia constant, s; and ω_b is the base rotor speed, rad/s.

Such an implementation allows to exclude the use of the phase-locked loop controller (PLL) in the control system, because instead of the grid frequency ω_g the reference frequency

value ω_{ref} is used, and therefore to exclude the inherent problems of PLL stability, especially in weak and ultra-weak grids [34]. However, despite the seeming effectiveness of the specified implementation, it has fundamental contradictions outlined in the introduction. Thus, the structural diagram of the active power control loop for the conventional VC-VSG structure has the form shown in Figure 2.

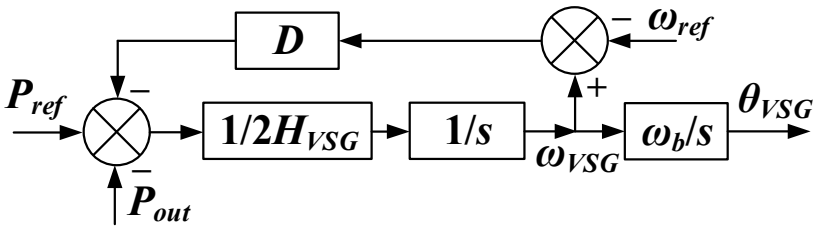

Figure 2. Active power control loop of the VC-VSG.

Since this paper proposes an approach to improve the VSG inertial response, it is sufficient to consider only the active power control loop. This loop forms the output active power and the frequency of the VSG, which directly affect the transients associated with grid frequency deviations. By evaluating the nature of changes in these variables, the shortcomings inherent in the conventional VC-VSG structure can be analyzed, and the merits of the proposed enhanced structure of the CC-VSG can be proven. In this regard, a closed-loop transfer function of the active power control loop is formed for each structure under consideration. For the VC-VSG, the scheme of such a function is shown in Figure 3, where k_s is the value of synchronizing power at zero angle δ_{VSG0} and is defined as $k_s = E_{VSG}U_g/L_g$ [35]. The consideration of the transfer function is the first step in the development of an adaptive algorithm because it allows for carrying out the analysis at the unit control level itself, i.e., to analyze a single-input and single-output system. This makes it possible to assess the impact of a particular parameter on a particular output value and also to assess the transient features of a particular loop in the control system.

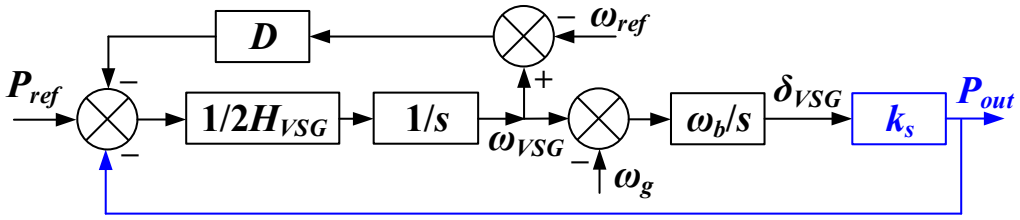

Figure 3. Scheme of the closed-loop transfer function of the active power control loop of the VC-VSG.

2.2. Enhanced CC-VSG Model

To exclude the previously indicated shortcomings of the VC-VSG, which prevent the application of effective adaptive approaches to control the virtual inertia and the damping coefficient, this paper proposes an enhanced structure of the CC-VSG [36,37]. The structural diagram of the considered CC-VSG is shown in Figure 4a. The peculiarity of this VSG-based control system is the use of two control loops for the formation of the desired CIG power references. The first loop determines the value of the main active and reactive power references P_{ref} and Q_{ref}, which can be set either from the generating unit control or from the plant level control. The second loop takes into account the electromagnetic and electromechanical equations of the VSG, resulting in the formation of values P_{VSG} and Q_{VSG}. The resulting values P_{ref}^* and Q_{ref}^* are formed by summing the values from the above two loops and are then used to determine the current references $i_{cvdqref}$ for the inner current control loop. The current control is configured with proportional-integral controllers with K_{pcc} and K_{icc} gains similar to the conventional VC-VSG. The VSG control within the considered CC-VSG structure is described according to (2)–(6) in the rotor

synchronous frame with the q-axis 90° leading the d-axis. Figure 4b depicts the power converter control time scale. As can be seen, the response time of the inner current control loop is often around tenths of ms, and that of the inertia control is more than ten times larger. Therefore, for the inertia control time scale dynamic analysis, the current control loop dynamic can be considered to instantaneously track its reference values.

$$\begin{cases} \frac{d\psi_d}{dt} = \omega_b\left(u_{od} + R_v i_{d,VSG} + \omega_{VSG}\psi_q\right) \\ \frac{d\psi_q}{dt} = \omega_b\left(u_{oq} + R_v i_{q,VSG} - \omega_{VSG}\psi_d\right) \end{cases} \tag{2}$$

$$\frac{d\psi_{1q}}{dt} = \omega_b\left(-R_{1q}i_{q,VSG} - \frac{R_{1q}}{L_{1q}}\psi_{1q}\right) = \frac{1}{\tau_{1q}}\left(-L_{1q}i_{q,VSG} - \psi_{1q}\right) \tag{3}$$

$$\frac{d\psi_{fd}}{dt} = K_u\left(\frac{Q_{set,VSG} - Q_{VSG}}{U_o}\right) \tag{4}$$

$$\begin{cases} i_{d,VSG} = \frac{\psi_{fd} - \psi_d}{L_v} \\ i_{q,VSG} = \frac{\psi_{1q} - \psi_q}{L_v} \end{cases} \tag{5}$$

$$\begin{cases} P_{VSG} = u_{od}i_{d,VSG} + u_{oq}i_{q,VSG} \\ Q_{VSG} = u_{oq}i_{d,VSG} - u_{od}i_{q,VSG} \end{cases} \tag{6}$$

where ψ_d, ψ_q, and ψ_{1q} are the virtual machine fluxes in d-q axes, R_{1q}, L_{1q}, and τ_{1q} are the virtual damper winding parameters, $Q_{ref,VSG}$ is the virtual machine reactive power reference, K_u is the reactive power control loop gain, u_{odq} are the terminal voltages in d-q axes, U_o is the rms voltage at the connection point of the LC-filter capacitance, and $i_{dq,VSG}$ are the virtual machine currents in d-q axes.

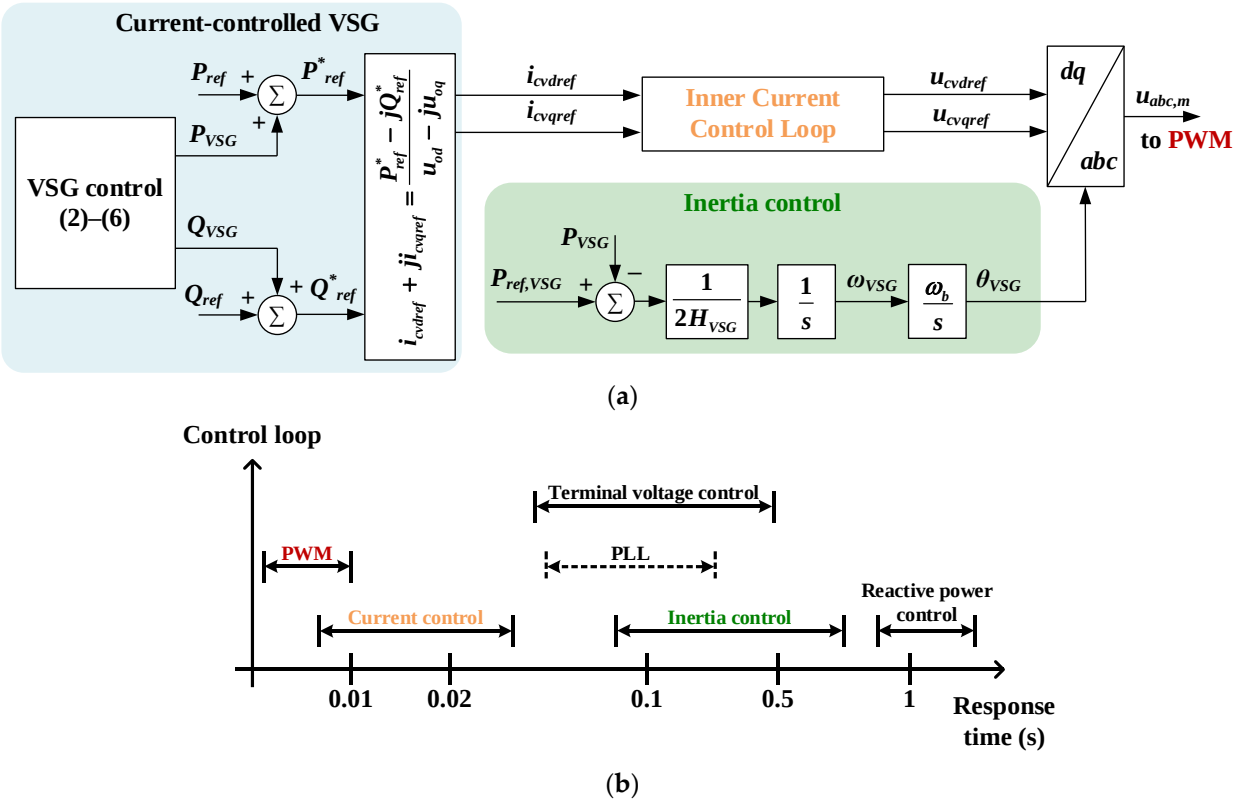

Figure 4. (**a**) Structural diagram of the CC-VSG and (**b**) control loops' time scale.

From Figure 4a, it follows that the main difference of the swing equation in the CC-VSG compared to the conventional VC-VSG structure is the absence of the damping coefficient D. Within the CC-VSG structure, the damping contribution is determined by a virtual damper winding, the quality of which depends on its parameters: time constant τ_{1q} and inductance L_{1q}, which are the analogue of the D coefficient. However, the described CC-VSG structure is PLL-free. The proposed VSG model is current-controlled, so the output parameters of the VSG model are the currents, and the input parameters for the control system are the voltages at the point of common coupling of the CIG. Accordingly, the equations describing the external grid have the following form (7) and (8) (the filter inductance L_f is taken into account in the grid inductance L_g):

$$\begin{cases} \frac{du_{od}}{dt} = \frac{\omega_b}{C_f} i_{cvd} - \frac{\omega_b}{C_f} i_{od} + \omega_b u_{oq} \\ \frac{du_{oq}}{dt} = \frac{\omega_b}{C_f} i_{cvq} - \frac{\omega_b}{C_f} i_{oq} - \omega_b u_{od} \end{cases} \tag{7}$$

$$\begin{cases} \frac{di_{od}}{dt} = \frac{\omega_b}{L_g} u_{od} - \frac{\omega_b}{L_g} U_g \sin\delta_{VSG} - \frac{\omega_b R_g}{L_g} i_{od} + \omega_b i_{oq} \\ \frac{di_{oq}}{dt} = \frac{\omega_b}{L_g} u_{oq} - \frac{\omega_b}{L_g} U_g \cos\delta_{VSG} - \frac{\omega_b R_g}{L_g} i_{oq} - \omega_b i_{od} \end{cases} \tag{8}$$

To form the closed-loop transfer function of the active power control loop of the CC-VSG, the linearization of Equations (1)–(8) around the steady-state operating point and the Laplace transform are performed. At the same time, a number of assumptions similar to the case of VC-VSG are to be used: (i) the resistances R_v and R_g are excluded, (ii) the steady-state operation is considered, i.e., $d\psi_q/dt = d\psi_d/dt = 0$ and $\omega_{VSG} = 1$, (iii) $P_{VSG0} = Q_{VSG0} = i_{d0,VSG} = i_{q0,VSG} = 0$, and (iv) the current control loop is excluded. The output active power of the converter P_{out}, taking into account the structure of the CC-VSG and the assumptions made, is as follows (9):

$$\begin{gathered} \Delta P_{out} = \Delta P_{VSG} + P_{ref} = \Delta u_{od} i_{cvd0} + u_{od0} \Delta i_{cvd} + \Delta u_{oq} i_{cvq0} + u_{oq0} \Delta i_{cvq} + P_{ref} \\ = U_o \sin(\delta_{VSG0}) \Delta i_{cvd} + U_o \cos(\delta_{VSG0}) \Delta i_{cvq} + P_{ref} = U_o \Delta i_{cvq} + P_{ref} \end{gathered} \tag{9}$$

The output power of the virtual generator is in turn determined by the following (10):

$$\begin{gathered} \Delta P_{VSG} = \Delta u_{od} i_{d0,VSG} + u_{od0} \Delta i_{d,VSG} + \Delta u_{oq} i_{q0,VSG} + u_{oq0} \Delta i_{q,VSG} \\ = U_o \sin(\delta_{VSG0}) \Delta i_{d,VSG} + U_o \cos(\delta_{VSG0}) \Delta i_{q,VSG} = U_o \Delta i_{q,VSG} \end{gathered} \tag{10}$$

It follows from (9) and (10) that it is only necessary to linearize the $i_{q,VSG}$ current Equation (10). As a result, Equation (11) is obtained:

$$\Delta i_{q,VSG} = \frac{\Delta\psi_{1q} - \Delta\psi_q}{L_v} \tag{11}$$

The virtual current along the q-axis depends on two fluxes. In order to find the increment of the virtual damper winding flux $\Delta\psi_{1q}$, the corresponding transformation of (3) is performed, and to find the increment of virtual stator flux along the q-axis $\Delta\psi_q$, the first equation of (2) is considered, taking into account the assumptions made. As a result, the Equations (12) and (13) are obtained, respectively:

$$\Delta\psi_{1q} = \frac{-L_{1q}}{1 + s\tau_{1q}} \Delta i_{q,VSG} \tag{12}$$

$$\Delta\psi_q = -\Delta U_{od} \tag{13}$$

where s is the Laplace operator.

In order to find ΔU_{od}, the first equation of (8) is linearized and the grid current i_o is expressed through the current at the converter terminals i_{cv}. As a result, Equation (14),

which depends on the increment of current Δi_{cv} and the angle $\Delta\delta_{VSG}$, is obtained. The last variable is found in the swing equation and is described by (15).

$$\begin{aligned}\Delta U_{od} &= \tfrac{1}{1-L_g C_f}\left[-L_g \Delta i_{cvq} + U_g \cos(\delta_{VSG0})\Delta\delta_{VSG}\right] \\ &= X_{C_f L_g}\left[-L_g \Delta i_{cvq} + U_g \cos(\delta_{VSG0})\Delta\delta_{VSG}\right]\end{aligned} \tag{14}$$

$$\Delta\delta_{VSG} = -\frac{\omega_b}{2H_{VSG}s^2}\Delta P_{VSG} \tag{15}$$

Combining (9)–(15), a closed-loop transfer function for the active power control loop is formed, the scheme of which is shown in Figure 5. This transfer function is obtained on the basis of the considered structure of the grid-connected VSG system (Figure 1) with the proposed CC-VSG control (Figure 4a) and can be divided into three parts: inertia control, virtual damper winding equations, and grid equations, which are obtained taking into account the assumptions given earlier.

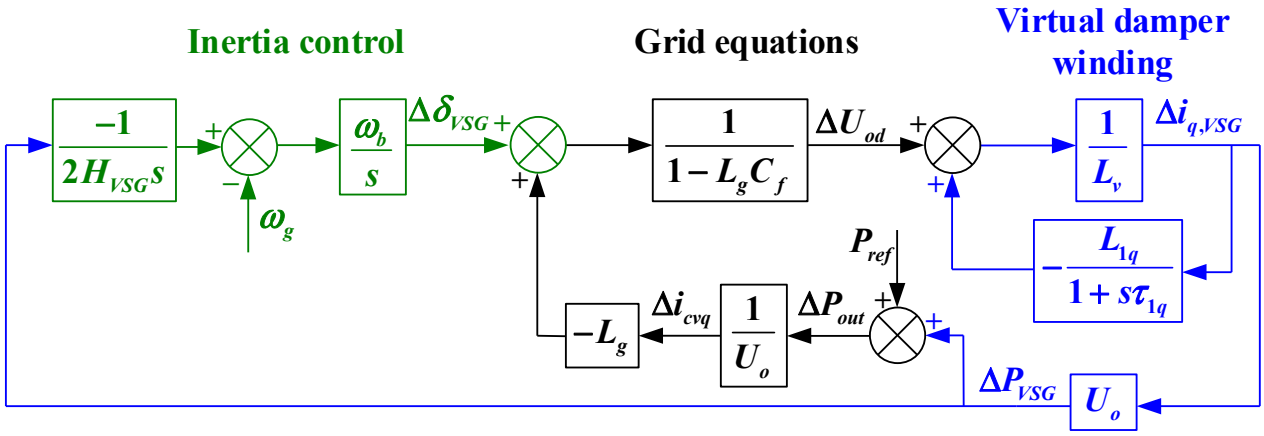

Figure 5. Scheme of the closed-loop transfer function of the active power control loop of the CC-VSG.

2.3. Differences in Dynamic Performances of the VC-VSG and CC-VSG Structures

To compare the features of the VC-VSG and CC-VSG models, the test grid shown in Figure 1 is used. From the obtained closed-loop transfer functions for the active power control loop of the VC-VSG and CC-VSG in Figures 3 and 5, it follows that there are two input variables P_{ref} and ω_g. Among the output variables, the main interests are ΔP_{out} and $\Delta\omega_{VSG}$, which directly determine the dynamic response of the system. These inputs/outputs are discussed below.

(1) $\Delta P_{out}/\Delta P_{ref}$. Based on Figure 3, the closed-loop transfer function from the input active power reference of the VC-VSG to the output active power is as follows (16):

$$G_{P/P\_VC-VSG}(s) = \frac{\Delta P_{out}}{\Delta P_{ref}} = \frac{\omega_b k_s}{2H_{VSG}s^2 + Ds + \omega_b k_s} \tag{16}$$

Equation (16) is a standard second-order system for which the main coefficients determining the dynamic properties of the system, the undamped natural frequency ω_n and the damping ratio ζ, are obtained by the well-known Formula (17):

$$\omega_{n\_VC-VSG} = \sqrt{\frac{k_s\omega_b}{2H_{VSG}}},\ \zeta_{VC-VSG} = \frac{D}{2\sqrt{2H_{VSG}k_s\omega_b}} \tag{17}$$

Based on Figure 5, a similar transfer function is made for the CC-VSG (18):

$$G_{P/P\_CC-VSG}(s) = \frac{\Delta P_{out}}{\Delta P_{ref}} = \frac{2H_{VSG}L_v\tau_{1q}s^3+2H_{VSG}\left(L_v+L_{1q}\right)s^2+U_0\omega_bX_{C_fL_g}\tau_{1q}s+U_0\omega_bX_{C_fL_g}}{2H_{VSG}\tau_{1q}\left(L_v+X_{C_fL_g}L_g\right)s^3+2H_{VSG}\left(L_v+L_{1q}+X_{C_fL_g}L_g\right)s^2+U_0\omega_bX_{C_fL_g}\tau_{1q}s+U_0\omega_bX_{C_fL_g}} \quad (18)$$

The characteristic equation of the $G_{P/P\_CC\text{-}VSG}(s)$ function is a third-degree polynomial, which can be expressed as follows (19):

$$as^3 + bs^2 + cs + d = 0 \quad (19)$$

where:

$$a = 2H_{VSG}\tau_{1q}\left(L_v + X_{C_fL_g}L_g\right),\ b = 2H_{VSG}\left(L_v + L_{1q} + X_{C_fL_g}L_g\right),\ c = U_0\omega_bX_{C_fL_g}\tau_{1q},\ d = U_0\omega_bX_{C_fL_g}.$$

Obviously, the third-order system can be represented as a series connection of a first-order lag function with a time constant T_1 and a second-order function having in the aggregate one real and two complex conjugate roots, respectively. The location of the roots of the characteristic equation and, correspondingly, the dynamic properties of $G_{P/P\_CC\text{-}VSG}(s)$ function depend on three coefficients: ζ, ω_n, and the time constant T_1.

For their determination, it is suitable to use parameters A and B of Vyshnegradskii's diagram, reflecting the stability of the third-order system [38,39]. For this purpose, Equation (19) is reduced to the normalized form (20) by dividing all terms of the equation by a free term and by introducing a new variable $q = s/\sqrt[3]{d/a}$.

$$q^3 + Aq^2 + Bq + 1 = 0 \quad (20)$$

where

$$A = \frac{b}{\sqrt[3]{a^2d}} = \sqrt[3]{\frac{2H_{VSG}\left(L_v+L_{1q}+L_gX_{C_fL_g}\right)^3}{{\tau_{1q}}^2U_0\omega_bX_{C_fL_g}\left(L_v+L_gX_{C_fL_g}\right)}}$$

$$B = \frac{c}{\sqrt[3]{ad^2}} = \sqrt[3]{\frac{U_0\omega_bX_{C_fL_g}{\tau_{1q}}^2}{2H_{VSG}\left(L_v+L_gX_{C_fL_g}\right)}}$$

For Equation (20), the coefficients of interest are obtained by the following Formula (21):

$$T_1 = \frac{Q}{\omega_n},\ \omega_n = \sqrt[3]{Q\frac{d}{a}},\ \zeta = \frac{A^3\sqrt{Q^2}-1}{2Q} \quad (21)$$

where $Q = \sqrt[3]{q}$ is a positive real root of the cubic equation $q^3 - Bq^2 + Aq + 1 = 0$.

The calculations based on (18)–(21) confirm that the damping properties of the CC-VSG depend on the parameters τ_{1q} and L_{1q}, which are analogue to the D coefficient in the conventional VC-VSG model (17). In addition, it is important to note that the transfer function (18) contains a third-degree polynomial in the numerator similar to the denominator, the zeros of which affect the quality of the transient performance. This polynomial will always have a coefficient before the high-order variable that is smaller than the same value in the denominator. This feature leads to the fact that the roots of the numerator, which will determine the rise time during the transients, will be the most distant to the imaginary axis.

Figure 6a shows the Bode plots of the closed-loop transfer function $\Delta P_{out}/\Delta P_{ref}$ for the conventional VSG structure. As noted earlier, the $G_{P/P\_VC\text{-}VSG}(s)$ function is a standard second-order system, and as the damping ratio ζ increases, the value of overshoot decreases (the Bode plots show that the resonance peak is being suppressed gradually by increasing the damping ratio). However, as is more important in the framework of the adaptive algorithms, the increase in damping is accompanied by a decrease in the bandwidth and, consequently, by a decrease in the response speed of the control system (rise time is inversely proportional to the bandwidth). As a result, in the case of adaptive change of

the damping coefficient D, it will be necessary to find a trade-off between the ability to suppress overshoot and the response speed of the control system.

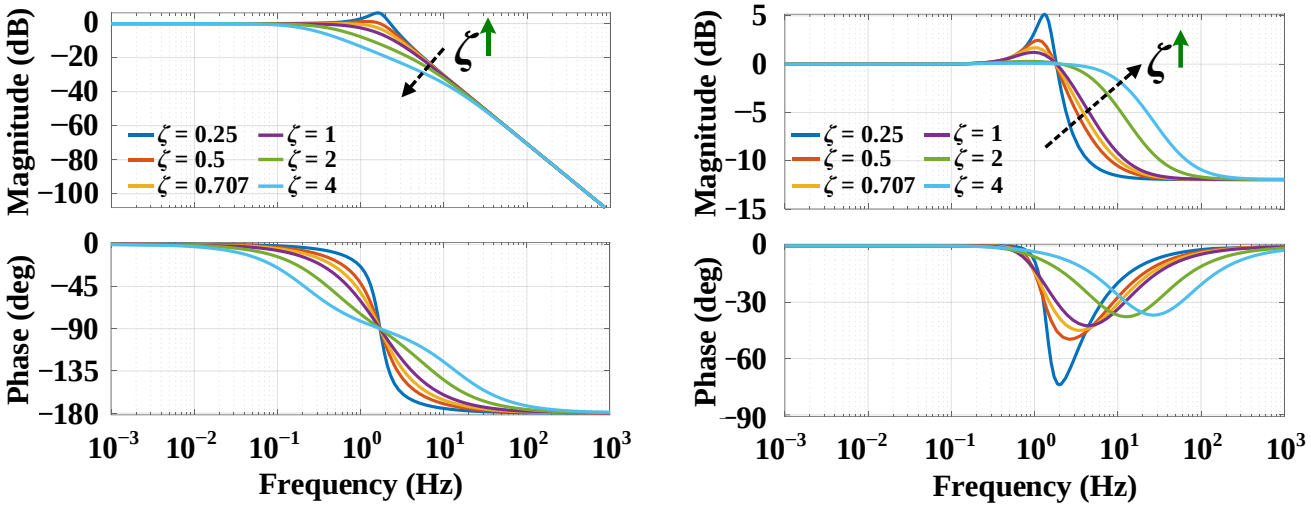

Figure 6. Bode plots of $G_{P/P}(s)$ with different damping ratios: (**a**) VC-VSG, (**b**) CC-VSG.

For the $G_{P/P\_CC\text{-}VSG}(s)$ function, an increase in the damping coefficient ζ similarly decreases the overshoot (Figure 6b). However, in contrast to the VC-VSG, an increase in ζ increases the bandwidth, which provides a faster dynamic response of the active power. This feature is related to the removal from the imaginary axis of one of the numerator roots as ζ increases. When ζ increases from 0 to 1, this root corresponds to a first-order lag function, and when $\zeta > 1$, to a second-order function, whose roots already become real. Thus, the increase in the damping properties of the CC-VSG due to τ_{1q} and L_{1q} increases the system's ability to suppress overshoot and increase the response speed when the active power reference changes, i.e., the system's dynamic response to changes in both active power and frequency improves simultaneously. Due to this feature of the CC-VSG, which solves the first of the three fundamental contradictions outlined in the introduction, an adaptive algorithm for controlling the damping properties of the system can be applied. Such an algorithm will make it possible to obtain a fast response of the active power without overshooting and low damping of the emerging oscillations. As a result, there is no need to introduce synthetic reduction of the damping coefficient in order to provide a trade-off between response speed and overshoot. The pattern of variation of τ_{1q} and L_{1q} to form the required damping ratio ζ is discussed in Section 3.

(2) $\Delta P_{out}/\Delta\omega_g$. The closed-loop transfer function for the considered control loops is given in (22) and (23):

$$G_{P/\omega\_VC-VSG}(s) = \frac{\Delta P_{out}}{\Delta\omega_g} = \frac{-\omega_b k_s (D + 2H_{VSG}s)}{2H_{VSG}s^2 + Ds + \omega_b k_s} \tag{22}$$

$$G_{P/\omega\_CC-VSG}(s) = \frac{\Delta P_{out}}{\Delta\omega_g} = \frac{-2H_{VSG}d(\tau_{1q}s^2 + s)}{as^3 + bs^2 + cs + d} \tag{23}$$

As can be seen from (22) and (23), the numerator of both transfer functions has changed. The differences appear in the location of the zeros of the transfer functions and their values in the steady-state. The Bode plots for the VC-VSG and CC-VSG are shown in Figure 7a,b, respectively. The obtained diagrams indicate a decrease in the magnitude at the resonant frequency with an increase in the damping ratio for both transfer functions. However, for the $G_{P/\omega\_VC\text{-}VSG}(s)$ function, when ζ increases, a similar increase in the steady-state value

of active power is observed (it is expressed in different values of the steady-state gain for the VC-VSG). This behavior of the system is due to the impact of the D coefficient on the frequency droop. In contrast, for the CC-VSG, the steady-state value of the output active power is independent of ζ.

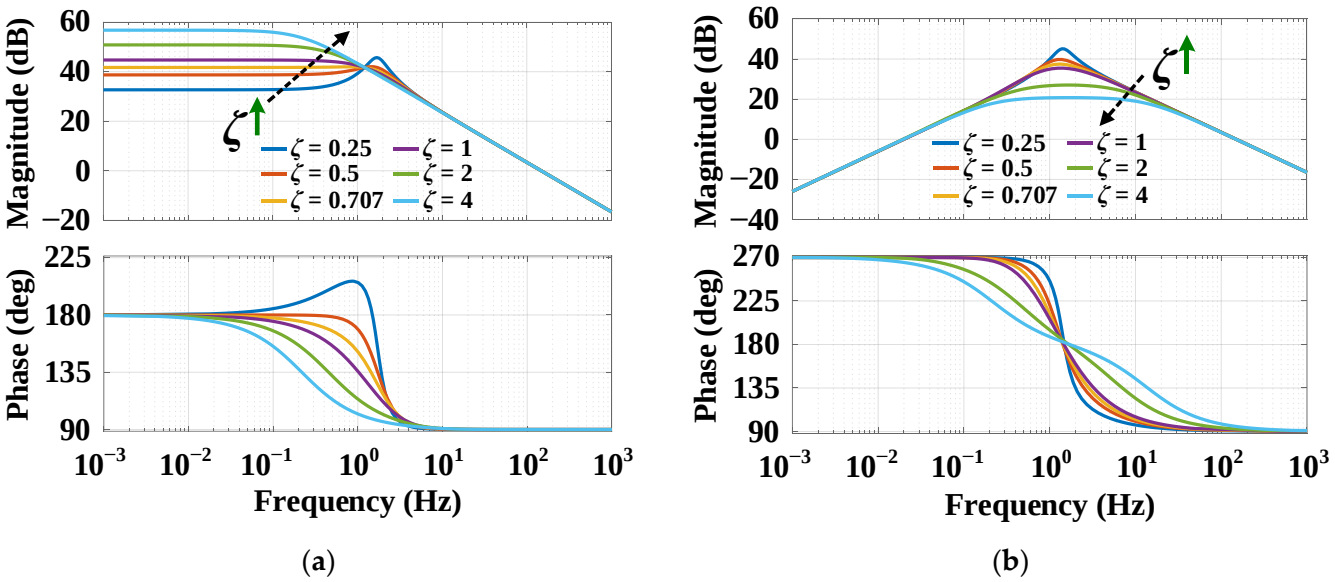

Figure 7. Bode plots of $G_{P/\omega}(s)$ with different damping ratios: (**a**) VC-VSG, (**b**) CC-VSG.

It was noted earlier that the output active power for both VSG structures depends on the input variables P_{ref} and ω_g. Consequently, the mathematical response of the active power can be represented using Equation (24):

$$P_{out} = G_{P/P}(s)P_{ref} - G_{P/\omega}(s)\Delta\omega_g \tag{24}$$

Using (24), the output active power in steady-state ($s = 0$) for both VSG models can be calculated as follows:

$$P_{out\_VC-VSG} = P_{ref} + D\Delta\omega_g \tag{25}$$

$$P_{out\_CC-VSG} = P_{ref} + 0\Delta\omega_g = P_{ref} \tag{26}$$

Comparing (25) and (26), it is obvious that as the D coefficient increases, the frequency droop increases, leading to an increase in the steady-state value of output active power for the VC-VSG. For the CC-VSG, the value of output active power is not connected with the damping properties of the system, and in case of the addition of droop coefficient will depend only on its value. Thus, the enhanced structure of the CC-VSG allows for solving the second of the three contradictions indicated in the introduction, which is related to the impact of the damping coefficient within the VC-VSG structure on the frequency droop.

(3) $\Delta\omega_{VSG}/\Delta\omega_g$. The closed-loop transfer functions from the grid frequency to the virtual generator frequency for the VC-VSG and CC-VSG have the form (27) and (28), respectively:

$$G_{\omega/\omega\_VC-VSG}(s) = \frac{\Delta\omega_{VSG}}{\Delta\omega_g} = \frac{\omega_b k_s}{2H_{VSG}s^2 + Ds + \omega_b k_s} \tag{27}$$

$$G_{\omega/\omega\_CC-VSG}(s) = \frac{\Delta\omega_{VSG}}{\Delta\omega_g} = \frac{d(\tau_{1q}s + 1)}{as^3 + bs^2 + cs + d} \tag{28}$$

The Bode plots for both functions (27) and (28) are shown in Figure 8. In this case, the frequency response of both control systems is the same. As can be seen, the value of overshoot decreases as the damping ratio increases. This also achieves a decrease in

the RoCoF and magnitude of frequency deviation. The zeros of the numerator of the $G_{\omega/\omega\_CC\text{-}VSG}(s)$ function do not have a significant impact on the quality of the transient performance. Thus, in this case, high values of the damping ratio are preferable for both the VC-VSG and the CC-VSG.

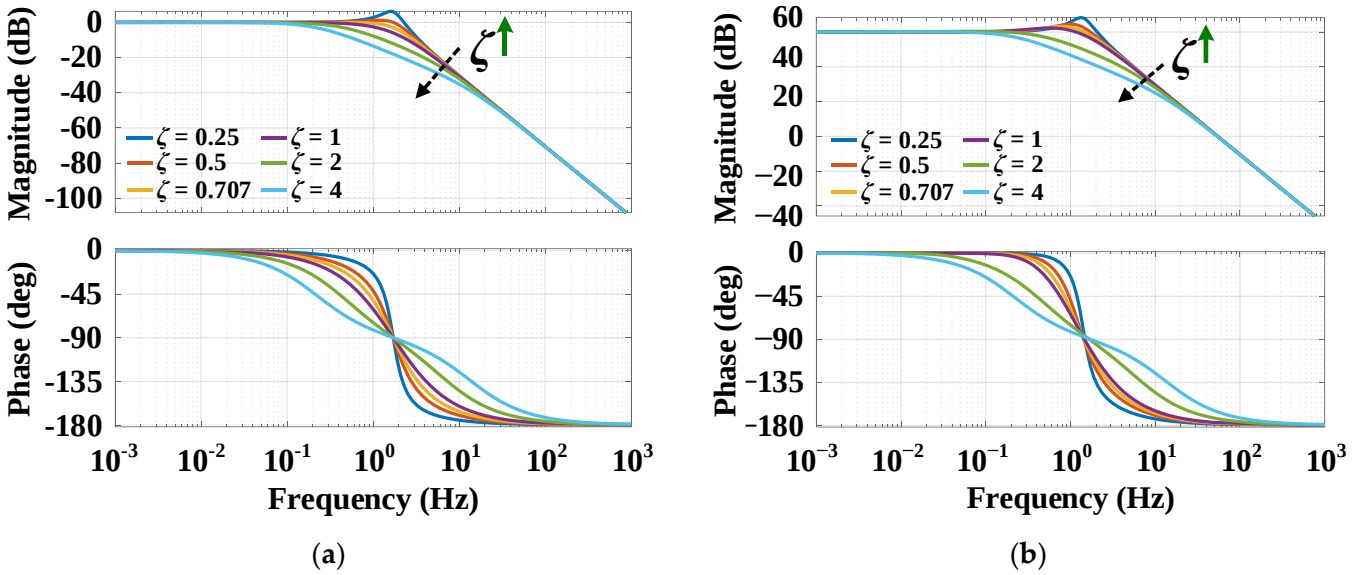

Figure 8. Bode plots of $G_{\omega/\omega}(s)$ with different damping ratios: (**a**) VC-VSG, (**b**) CC-VSG.

Summarizing the dynamic properties of the control systems under the changes in the active power and grid frequency, it follows that, in contrast to the conventional structure of VC-VSG, the proposed structure of CC-VSG allows simultaneously providing a fast response of the output active power and a slow response under the changes in the grid frequency. In the case of an adaptive change of the damping coefficient D for the VC-VSG, the response speed of the active power and frequency changes in one direction, i.e., the response of the frequency and active power will be either slow or fast at the same time. In this case, it becomes necessary to determine the control priority: either in active power or in frequency. Such behavior of the control system is undesirable because the quality of the transient performance inevitably decreases, and the adaptive control does not provide a significant positive impact. Thus, by using the proposed CC-VSG, the third contradiction is solved, which consists of the need to find a trade-off between the active power control and the frequency control.

Based on the presented theoretical analysis, it follows that in the case of using the proposed structure of CC-VSG, the adaptive algorithms can be applied to flexibly change the control system parameters: H_{VSG}, L_{1q}, and τ_{1q}. By changing them, it becomes possible to achieve the desired quality of the transient process, regardless of its stage of occurrence and its causes. The latter is determined by the absence of contradictions in the impact of these coefficients on the dynamic response of the control system.

3. Impacts of Virtual Inertia and Damping Coefficient on the Dynamic Response of the CC-VSG under Disturbances

During the development of an adaptive algorithm for changing the parameters of the CC-VSG, it is necessary to understand the impact of these parameters on the dynamic response of the system. Therefore, for a visual comprehension of the resulting relationships, it is suitable to use the transient functions in the time domain. In this regard, the closed-

loop transfer function from the input active power ΔP_{ref} to the virtual generator frequency $\Delta\omega_{VSG}$ (29) is written and the inverse Laplace transform (30) is used:

$$G_{\omega/P\_CC-VSG}(s) = \frac{\Delta\omega_{VSG}}{\Delta P_{ref}} = \frac{X_{C_f L_g} L_g s(\tau_{1q} s + 1)}{as^3 + bs^2 + cs + d} \tag{29}$$

$$\Delta\omega_{VSG}(t) = \frac{e^{-\zeta\theta}\sinh(\varepsilon\theta)(T_2 k_1 - QT_2 k_1 \zeta + Qk_2 - \zeta k_2) - \varepsilon\left[e^{-\theta/Q} - e^{-\zeta\theta}\cosh(\varepsilon\theta)\right](k_2 - k_1 QT_2)}{T_2^2 \varepsilon(Q^2 - 2\zeta Q + 1)} \tag{30}$$

where $\varepsilon = \sqrt{\zeta^2 - 1}$, $\theta = t \cdot \omega_n$, $T_2 = 1/\omega_n$, $k_2 = X_{C_f L_g} L_g \tau_{1q}$, $k_1 = X_{C_f L_g} L_g$.

Under disturbances, the response of the CC-VSG is similar to the behavior of conventional synchronous generation and is described by the well-known power-angle curve [24]. On this curve, it is common to identify four characteristic stages emerging under a disturbance: the first and third are associated with the acceleration of the virtual rotor, and the second and fourth with its deceleration [18]. The transition from one stage to another is easily determined by comparing the deviation of the VSG angular frequency $\Delta\omega_{VSG}$, rate of change $d\omega_{VSG}/dt$, and their product with zero [26]. Each of these stages corresponds to a different adaptive control objective.

Based on the swing equation used in the CC-VSG (Figure 4a), it follows that the virtual inertia H_{VSG} is inversely proportional to the rate of change of angular frequency $d\omega_{VSG}/dt$. Consequently, during the acceleration stage, a larger value of H_{VSG} is required to reduce both the magnitude of the frequency deviation and RoCoF. In contrast, during the deceleration stage, the magnitude of angular frequency deviation is at its maximum and a small value of H_{VSG} is required to recover the angular frequency to its steady-state value as quickly as possible. Figure 9 shows the transient characteristics for (30) at different values of H_{VSG}, which confirm the conclusions made and define the objective of the adaptive change in the virtual inertia at each of the outlined stages.

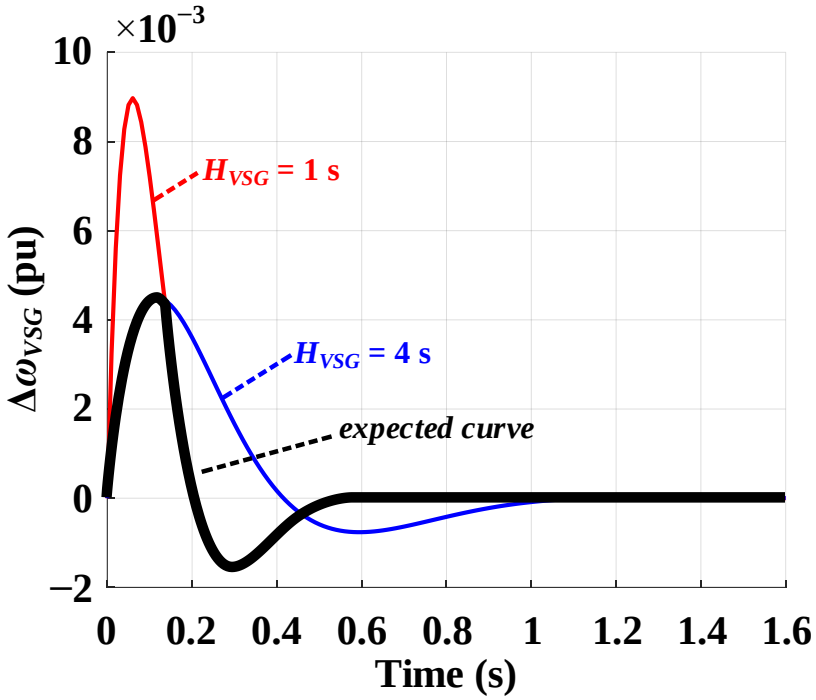

Figure 9. The angular frequency deviation under different virtual inertia values.

As indicated earlier, for the developed CC-VSG structure, the degree of damping depends on two coefficients: the time constant τ_{1q} and the inductance L_{1q} of the virtual damper winding. Their impact on the dynamic response is determined by the characteristic

equation of the transfer function $G_{\omega/P\_CC\text{-}VSG}(s)$, which is a third-degree polynomial. This equation can be considered on the *A*–*B* plane (Figure 10), through which τ_{1q} (31) and L_{1q} (32) are expressed:

$$\tau_{1q} = \sqrt[3]{\frac{B^3 2H_{VSG}\left(L_v + L_g X_{C_f L_g}\right)}{U_o X_{C_f L_g} \omega_b}} \tag{31}$$

$$L_{1q} = -L_v - L_g X_{C_f L_g} + A\sqrt[3]{\frac{\tau_{1q}^2\left(L_v + L_g X_{C_f L_g}\right) U_o X_{C_f L_g} \omega_b}{2H_{VSG}}} \tag{32}$$

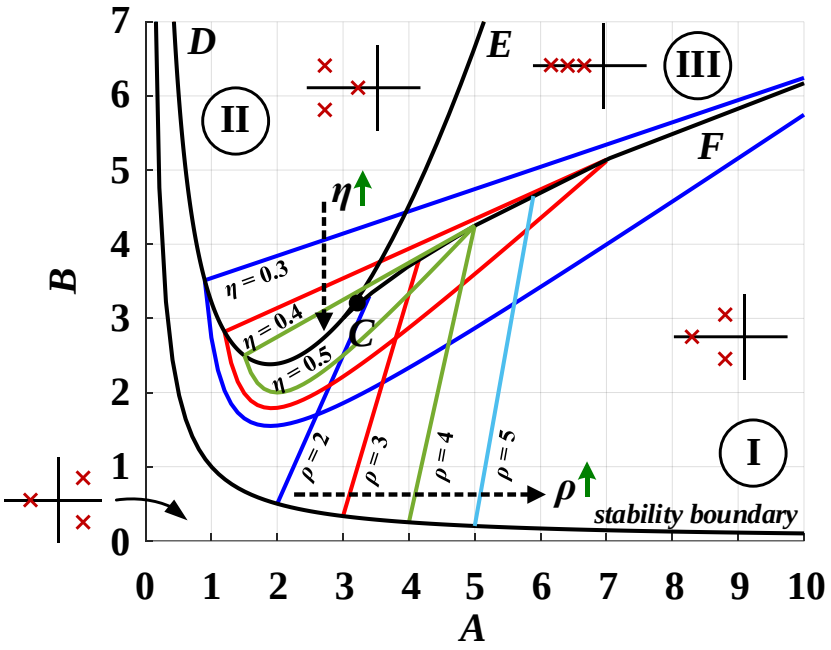

Figure 10. Vyshnegradskii's stability diagram in the *A*–*B* plane.

The main objective of the damping loop is to provide effective oscillations damping and stability of the system in general. Based on this objective, the adaptive control is carried out within the framework of the conventional VC-VSG structure [40]. However, due to the proposed enhanced structure of the CC-VSG, it is possible to increase the degree of freedom of the system, and by changing the two parameters associated with damping, to affect another dynamic characteristic of the system, thereby significantly improving the quality of the transient process. In this regard, during the acceleration stage, in addition to increasing the damping, it is necessary to reduce the rise time, which contributes to reducing the maximum deviation and the rate of the change of frequency. For this purpose, a point in the *ECF* area must be selected within which the condition $\zeta \geq 1$ is always satisfied (Figure 10). The limitation of the rise time is achieved by reducing the time constant T_1 of the first-order lag function, which corresponds to the moving of the real root $\rho = -1/T_1$ of the characteristic Equation (29) from the imaginary axis. The real root must be to the left of the complex conjugate roots on the complex plane, which corresponds to the area I in Figure 10. In accordance with the indicated conditions on the *A*–*B* plane, the movement of the real root to the left corresponds to the movement to the right of the lines of equal maximal absolute values of the root furthest from the imaginary axis, which are described by Equation (33):

$$B = 1/\rho + A\rho - \rho^2 \tag{33}$$

At the deceleration stage, in order to maintain the damping ratio $\zeta \geq 1$, it is necessary to provide a high decay rate of the transient process, which will correspond to a rapid

recovery of the virtual rotor angular frequency to the steady-state value. For this purpose, it is necessary to increase the absolute value of the real part of the complex conjugate roots, which corresponds to the lines of equal response speed (η) in Figure 10 and is depicted by Equation (34):

$$\begin{cases} B = A\eta - \eta^2 + 1/\eta \\ B = 1/(A - 2\eta) + 2\eta(1 - 2\eta) \end{cases} \quad (34)$$

The hypotheses made about the parameters' impact on the dynamic response of the system are confirmed by the obtained transient characteristics in the time domain (30). Figure 11a shows two points with different values of A and B. The transient characteristics in Figure 11b prove that the selection of Point 2 on the CF line, corresponding to a larger value of ρ, allows achieving a smaller deviation magnitude and rate of change of the VSG frequency, which is the major objective of adaptive control at the acceleration stage.

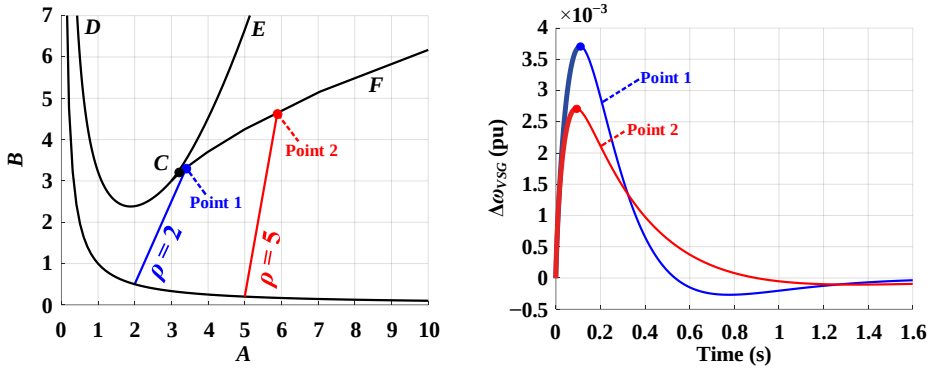

(**a**) (**b**)

Figure 11. (**a**) Vyshnegradskii's diagram with different values of ρ; (**b**) transient characteristics of the angular frequency deviation, corresponding to the Points 1 and 2 and considered during the acceleration stage.

Figure 12a shows Points 1 and 2, which are characteristic of the deceleration stage. The transient response in the time domain in Figure 12b proves that the selection of Point 2 with a larger value of η contributes to a more rapid recovery of the angular frequency to the steady-state value. Thus, by selecting the necessary values of A and B and corresponding $\tau_{1\eta}$ and $L_{1\eta}$ at each stage of the transient process, it is possible to obtain the desired characteristics of the dynamic response of the developed CC-VSG structure.

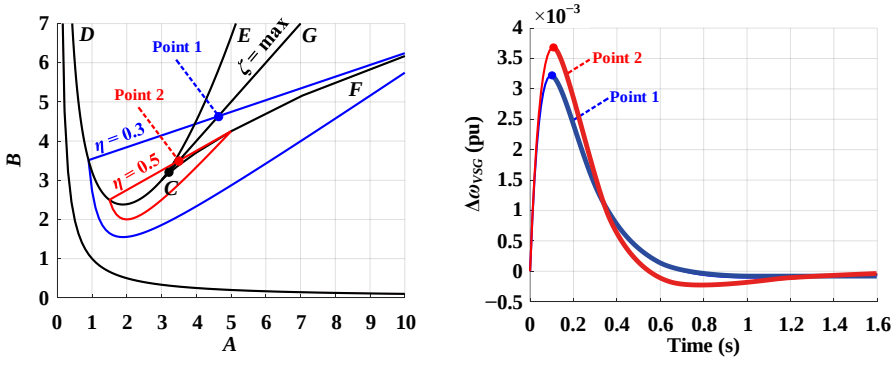

(**a**) (**b**)

Figure 12. (**a**) Vyshnegradskii's diagram with different values of η; (**b**) transient characteristics of the angular frequency deviation, corresponding to Points 1 and 2 and considered during the deceleration stage.

4. Adaptive Adjustment Strategy for the CC-VSG

4.1. Proposed Adaptive Virtual Inertia Control

In accordance with the logic and objectives of the adaptive control of VSG parameters given in Section 3, this section describes the proposed implementation of the adaptive algorithm for changing the virtual inertia, which is based on the nonlinear sigmoid function (35):

$$H_{VSG} = \left(H_0 - \frac{H_0 \cdot k_{H1}}{2} \right) + \frac{H_0 \cdot k_{H1}}{1 + \exp\left[-k_{H2} \cdot \left[df_{VSG}/dt \cdot \left(\Delta f_{VSG} + k_{H3} \cdot k_{H4} \cdot \left| df_{VSG}/dt \right| \right) \right] \right]} \tag{35}$$

where H_0 is the inertia constant of the VSG in the normal steady-state, s; $\Delta f_{VSG} = f_{VSG} - f_0$ is the deviation of the VSG frequency f_{VSG} from the reference value f_0, where $f_{VSG} = \omega_{VSG}/2\pi$, Hz; df_{VSG}/dt is the rate of change of VSG frequency, Hz/s, and $k_{H1–H4}$ are the coefficients of the adaptive function.

From (35), it follows that only information about the current values of the VSG frequency f_{VSG} and its RoCoF df_{VSG}/dt are used for the proposed adaptive control of the VSG virtual inertia H_{VSG}. The advantage of the proposed approach is the use of f_{VSG} and df_{VSG}/dt directly from the swing equation within the inertia control, taking into account the corresponding transformations, without the need for a PLL controller to measure the frequency and a derivative function to determine the RoCoF, which can lead to the CIG instability.

The value of H_0 is set on the basis of the maximum value of VSG inertia $H_{\max}$, which is determined by the capacitance of the DC bus (36) and is calculated according to Equation (37):

$$H_{\max} = \frac{C_{DC} U_{DC}^2}{2 S_n} \tag{36}$$

$$H_0 = 0.5 H_{\max} \tag{37}$$

where C_{DC} is the capacitance of the DC bus, F; U_{DC} is the DC bus reference voltage, V; and S_n is the converter rated power, VA.

At the same time, the minimum value of the VSG inertia $H_{\min}$ should also be limited to a value close to zero (e.g., $H_{\min}$ = 0.1 s) to avoid dividing by zero in the VSG swing equation.

The coefficient k_{H1} determines the ranges in which the value of H_{VSG} will change under disturbances with the ability to account for the rate of change of frequency $\mathrm{RoCoF_{set}}$. This coefficient is defined on the basis of the cubic function (38):

$$k_{H1} = \begin{cases} 2 \cdot \left(H_{\max}/H_0 - 1 \right) & \text{if } a_H + b_H \cdot c_H \cdot \left(df_{VSG}/dt \right)^3 > 2 \cdot \left(H_{\max}/H_0 - 1 \right) \\ a_H + b_H \cdot c_H \cdot \left(df_{VSG}/dt \right)^3 & \text{if } 2 \cdot \left(1 - H_{\max}/H_0 \right) \le a_H + b_H \cdot c_H \cdot \left(df_{VSG}/dt \right)^3 \le 2 \cdot \left(H_{\max}/H_0 - 1 \right) \\ 2 \cdot \left(1 - H_{\max}/H_0 \right) & \text{if } a_H + b_H \cdot c_H \cdot \left(df_{VSG}/dt \right)^3 < 2 \cdot \left(1 - H_{\max}/H_0 \right) \end{cases} \tag{38}$$

In Equation (38), the coefficient a_H determines the initial value of the coefficient k_{H1} when RoCoF is equal or close to zero. This forms the initial range $\{H_{\max}; H_{\min}\}$ for the change in the VSG inertia constant. The value of the coefficient a_H is chosen in the following range (39):

$$1 \le a_H \le 2 \cdot \left(H_{\max}/H_0 - 1 \right) \tag{39}$$

The coefficient b_H determines the sign of the cubic function based on the VSG frequency deviation (40), which is necessary for the proper operation of the algorithm at different stages of the transient process.

$$b_H = \text{sign}(f_{VSG} - f_0) \tag{40}$$

The coefficient c_H allows for changing the form of the function for k_{H1} with respect to the $\text{RoCoF}_{\text{set}}$ (Hz/s), which helps the algorithm for the VSG adaptive inertia to take into account the limitations on the value of RoCoF throughout the transient process. The value of this coefficient is derived according to Equation (41):

$$c_H = \begin{cases} \dfrac{2 \cdot \left(H_{\max} / H_0 - 1 \right) - a_H}{\text{RoCoF}_{\text{set}}^3} & \text{if } k_{H1} \geq a_H \\ \dfrac{a_H - 2 \cdot \left(1 - H_{\max} / H_0 \right)}{\text{RoCoF}_{\text{set}}^3} & \text{if } k_{H1} < a_H \end{cases} \tag{41}$$

The proposed algorithm also assumes the possibility of excluding the RoCoF control by setting a large value of $\text{RoCoF}_{\text{set}}$. In this case, the H_{VSG} variation range is determined only by the coefficient a_H in (38).

The resulting plot of the coefficient k_{H1} is shown in Figure 13, where curve 1 corresponds to the case with $\Delta f_{VSG} \geq 0$ and curve 2 corresponds to $\Delta f_{VSG} < 0$. At the same time, since the coefficient k_{H1} can be either greater or less than zero, the sigmoid function for controlling the VSG virtual inertia can be of two types (curve 1 with $k_{H1} \geq 0$ or curve 2 with $k_{H1} < 0$), as shown in Figure 14.

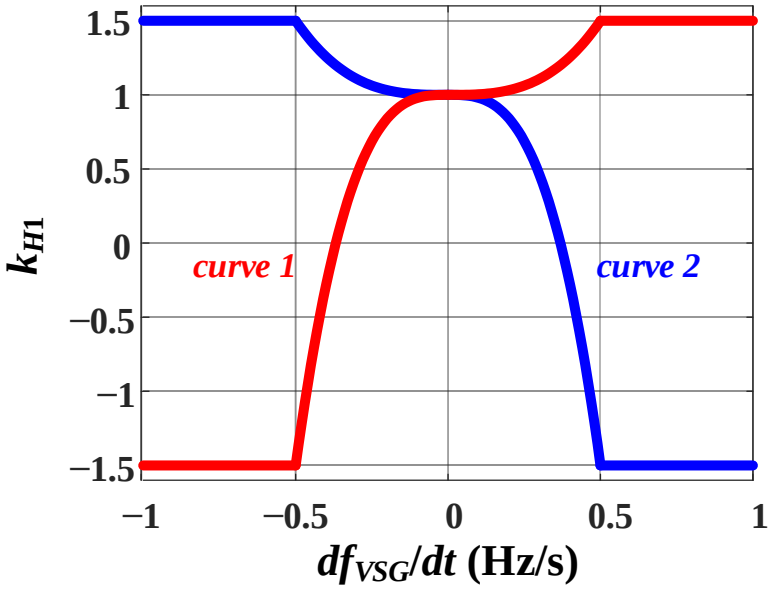

Figure 13. Variable k_{H1} coefficient.

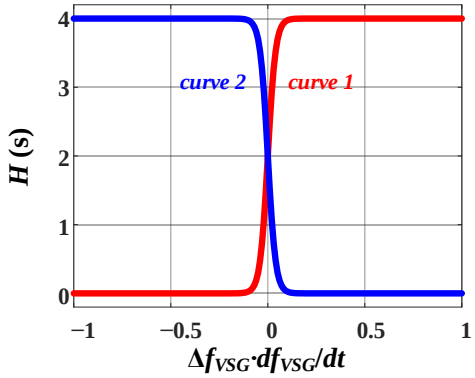

Figure 14. Plot of change in virtual inertia of the VSG.

In the above Equation (35) for the adaptive virtual inertia, the coefficients k_{H2}, k_{H3}, and k_{H4} are used to enhance the dynamic response of the CIG during the transients. The coefficient k_{H2} is necessary to increase the sensitivity of the adaptive inertia algorithm at the stage of oscillation damping by changing the slope of the sigmoid function. This coefficient is obtained by Equation (42):

$$k_{H2} = d_H + \left[-m_H + \frac{2 \cdot m_H}{1 + \exp(-n_H \cdot |\Delta f_{VSG}|)} \right] \tag{42}$$

The coefficient d_H defines the initial value of the coefficient k_{H2} and, accordingly, the initial slope of the sigmoid (35). This slope generally defines the system response to the value of Δf_{VSG} and df_{VSG}/dt. When the oscillation damping starts, the control of virtual inertia by the sigmoid function may not be sensitive enough in comparison with the conventional bang–bang control. In this regard, the increase in the slope of the sigmoid depending on Δf_{VSG}, as seen from (42), allows for improvement in the damping process when frequency deviations are still large enough but at the same time do not lead to undesirable VSG inertia switching when small deviations occur. Consequently, the coefficient m_H defines the degree of increase in the coefficient k_{H2} for large frequency deviations. The coefficient n_H defines the slope of the characteristic for the coefficient k_{H2}. Thus, the value of sensitivity to frequency deviations Δf_{VSG} is set. The resulting plot of the coefficient k_{H2} is shown in Figure 15.

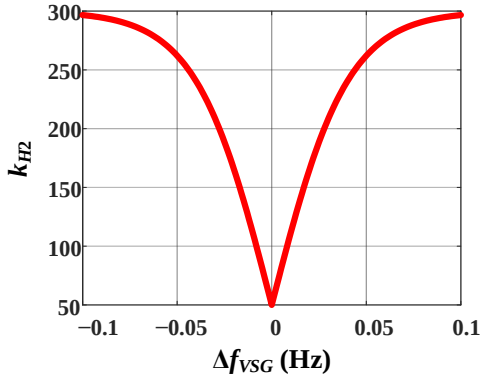

Figure 15. Variable k_{H2} coefficient.

The use of the virtual inertia relationship on a complex combination of parameters Δf_{VSG} and df_{VSG}/dt in (35), in contrast to the conventional approach, where only their product is used [41], is due to the need to exclude the excessive change in the H_{VSG} inertia to H_0, when the frequency deviation Δf_{VSG} crosses zero. The latter can lead to an undesirable sharp increase in RoCoF at these moments, as shown in Figure 16.

Such a problem can occur if there is a RoCoF limitation at the frequency recovery stage, due to which the value of H_{VSG} inertia becomes greater than H_0. In the conventional approach without a RoCoF limitation in the adaptive virtual inertia algorithm, a change in the sign of Δf_{VSG} is always followed by a change in H_{VSG} from a small value ($H_{VSG} < H_0$) to a large value ($H_{VSG} > H_0$) [25]. In the proposed algorithm, in this case, it is necessary, at the current high value of inertia, to remain at a value greater than H_0, without excessive reduction of inertia to H_0, since if $\Delta f_{VSG} = 0$ and $k_{H3} = k_{H4} = 0$, then $H_{VSG} = H_0$ according to (35). A similar performance of the adaptive inertia algorithm can be achieved by using, together with Δf_{VSG}, an additional term in the form of df_{VSG}/dt, where the coefficient k_{H3} defines the necessary sign of the term (43), and the weight coefficient k_{H4} defines the level of its impact (44).

$$k_{H3} = \text{sign}(f_{VSG} - f_0) \tag{43}$$

$$k_{H4} = \frac{df_{VSG}/dt^2}{df_{VSG}/dt^2 + \Delta f_{VSG}{}^2 + 1} \tag{44}$$

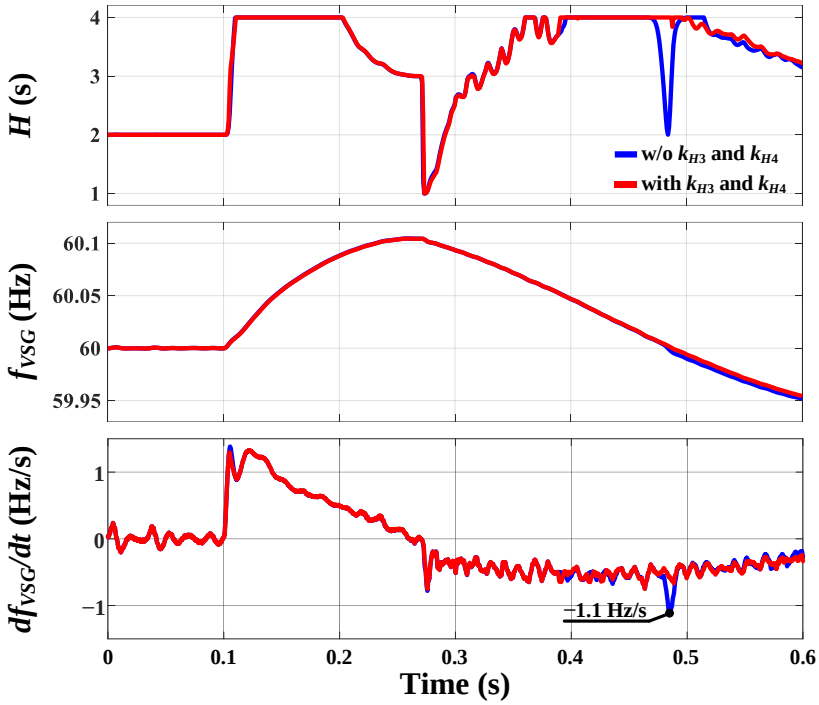

Figure 16. The impact of VSG inertia changes on RoCoF at different variants of sigmoid function implementation.

Therefore, due to the coefficient k_{H3}, the addition to Δf_{VSG} in the form of df_{VSG}/dt has the same sign as the current value of Δf_{VSG}, which does not lead to a divergence in the adaptive inertia algorithm of the VSG. The change in the coefficient k_{H4} according to the values of df_{VSG}/dt and Δf_{VSG} is shown in Figure 17. When Δf_{VSG} is close to zero and df_{VSG}/dt has a sufficiently large value, the coefficient $k_{H4} > 0$ and the addition of df_{VSG}/dt to Δf_{VSG} is performed, which allows to exclude that the exponent index at $\Delta f_{VSG} = 0$ is zero for the considered sigmoid function (35). At large values of Δf_{VSG}, the value of df_{VSG}/dt tends to zero; hence, the coefficient kH4 also tends to zero and does not affect the performance of the algorithm.

Summarizing the above, the principle of operation of the proposed adaptive virtual inertia algorithm is shown in Figures 18 and 19. When the VSG frequency deviation occurs

($\Delta f_{VSG} > 0$) and its rate of change increases ($df_{VSG}/dt > 0$) up to the moment when the RoCoF reference is exceeded, an appropriate increase in both the virtual inertia ($H_{VSG} > H_0$) and the coefficient k_{H1} occurs (points $a \rightarrow a_1$ in Figure 18). The latter allows increasing the H_{VSG} range, which contributes to reducing both the magnitude of the frequency deviation and RoCoF. Then H_{VSG} is equal to $H_{\max}$, as k_{H1} is equal to maximum value, until df_{VSG}/dt becomes less than the RoCoF reference ($a_1 \rightarrow a_2$). After the mentioned moment, k_{H1} starts decreasing with df_{VSG}/dt, which reduces the H_{VSG} range and, consequently, the current value of the virtual inertia ($a_2 \rightarrow b$). The next stage is frequency recovery, due to which the VSG inertia decreases to a minimum value ($H_{VSG} < H_0$). However, since the value of RoCoF increases when the inertia decreases, in order to limit it to the reference value $\text{RoCoF}_{\text{set}}$, the coefficient k_{H1} decreases and its sign changes ($b \rightarrow b_1$). Thus, H_{VSG} starts to increase. As a result, there may be some exceeding of $\text{RoCoF}_{\text{set}}$ due to reaching the maximum control capability of the CIG. Similar to the previously mentioned, H_{VSG} remains equal to $H_{\max}$, as k_{H1} is equal to minimum value, until df_{VSG}/dt becomes less than $\text{RoCoF}_{\text{set}}$ ($b_1 \rightarrow c$). After the change of sign $\Delta f_{VSG} < 0$ there is an appropriate increase of the coefficient k_{H1} up to the maximum value due to the requirement of $H_{VSG} > H_0$ at this stage of the transient process. Then, k_{H1} begins to decrease, which sequentially decreases the H_{VSG} ($c \rightarrow d$). When the sign of df_{VSG}/dt changes ($df_{VSG}/dt > 0$), the virtual inertia decreases ($H_{VSG} < H_0$). However, in order to prevent exceeding the $\text{RoCoF}_{\text{set}}$, the coefficient k_{H1} starts to change depending on the controlled df_{VSG}/dt value, which can lead to an inverse increase in inertia H_{VSG} ($d \rightarrow e$). The described process continues until the nominal VSG frequency is reached. Table 1 summarizes the operation of the proposed algorithm.

4.2. Proposed Adaptive Virtual Damper Winding Control

In order to maximize the performance of the CC-VSG in the case of grid frequency deviations, in addition to the adaptive virtual inertia control, an adaptive change in the parameters of the virtual damper winding (τ_{1q} and L_{1q}) is also proposed. The operating principle of the proposed adaptive algorithm is based on changing the coefficients A and B in (31) and (32) that are used to determine the necessary values of τ_{1q} and L_{1q}. As can be seen from (31) and (32), the values of the control system variables (H_{VSG}, L_v and ω_b) and the network parameters (C_f, L_g and U_o) are required to calculate the parameters of the virtual damper winding. Regarding the first set of data, there are no difficulties—the parameters of the control system are known. Meanwhile, the virtual inertia H_{VSG}, given the proposed adaptive control in Section 4.1, becomes a time-varying variable that can then be used to calculate τ_{1q} and L_{1q}. The value of the output filter capacitance C_f is a pre-calculated parameter and does not change during the converter operation. In order to determine the current equivalent grid inductance L_g, it is possible to use its online estimation according to various algorithms currently proposed [42]. In addition, the delays in measuring U_o should be taken into account. The studies on the operation of the proposed adaptive CC-VSG control and its optimization on the example of practical grid operating conditions, taking into account the online impedance estimation and delays in the voltage measurement, will be the scope of future work. Thus, in this paper it was taken into account that the parameter L_g is known, and the voltage U_o is entered into the control algorithm without any delays.

The selection of certain coefficients A and B to achieve the required dynamic response is made on the basis of the theoretical analysis given in Section 3. In normal steady-state, in order to provide high stability margins and damping ratio ($\zeta \approx 1$), as well as the response speed of the system ($\eta \approx 1$), the optimal solution is to locate at the point with coefficients $A = 3$ and $B = 3$ (Figure 10). When a VSG frequency deviation occurs, to ensure the smallest RoCoF value at the first stage of the transient, the system response speed must be reduced, but the damping ratio and stability margins must also be high. To achieve these properties, it is necessary to move to the right along the line CF (Figure 10), e.g., to the point with coefficients $A = 25$ and $B = 9$. After that, in order to reduce the magnitude of VSG frequency deviation, under the condition of fast frequency recovery while maintaining a

high damping ratio and the smallest overshoot, moving right along the line *CG* (Figure 12) into the area of aperiodic processes with $\zeta > 1$ (e.g., $A = 4$ and $B = 4$) is effective.

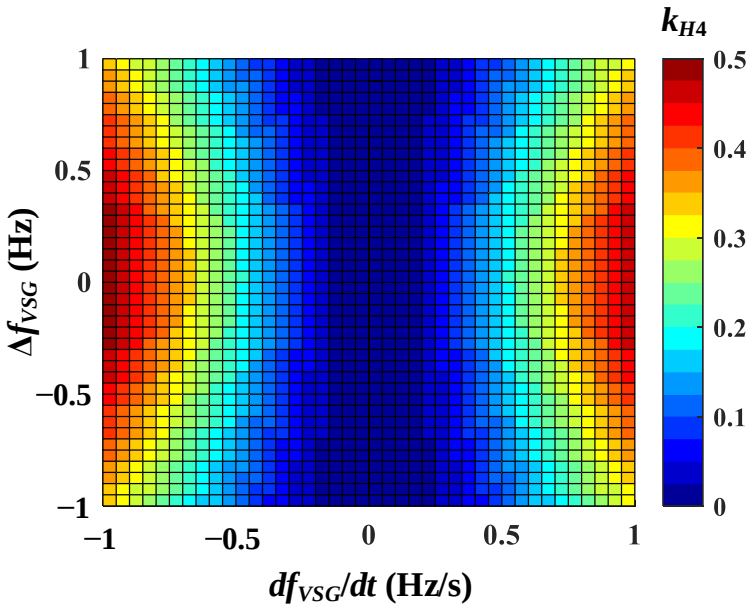

Figure 17. Variable k_{H4} coefficient.

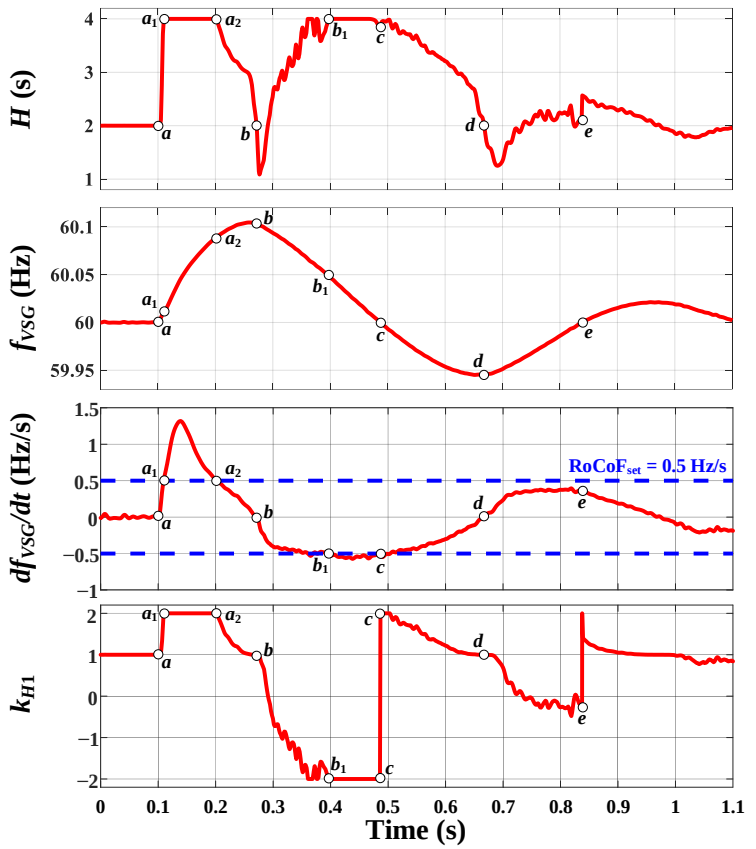

Figure 18. Operation of the proposed adaptive virtual inertia control.

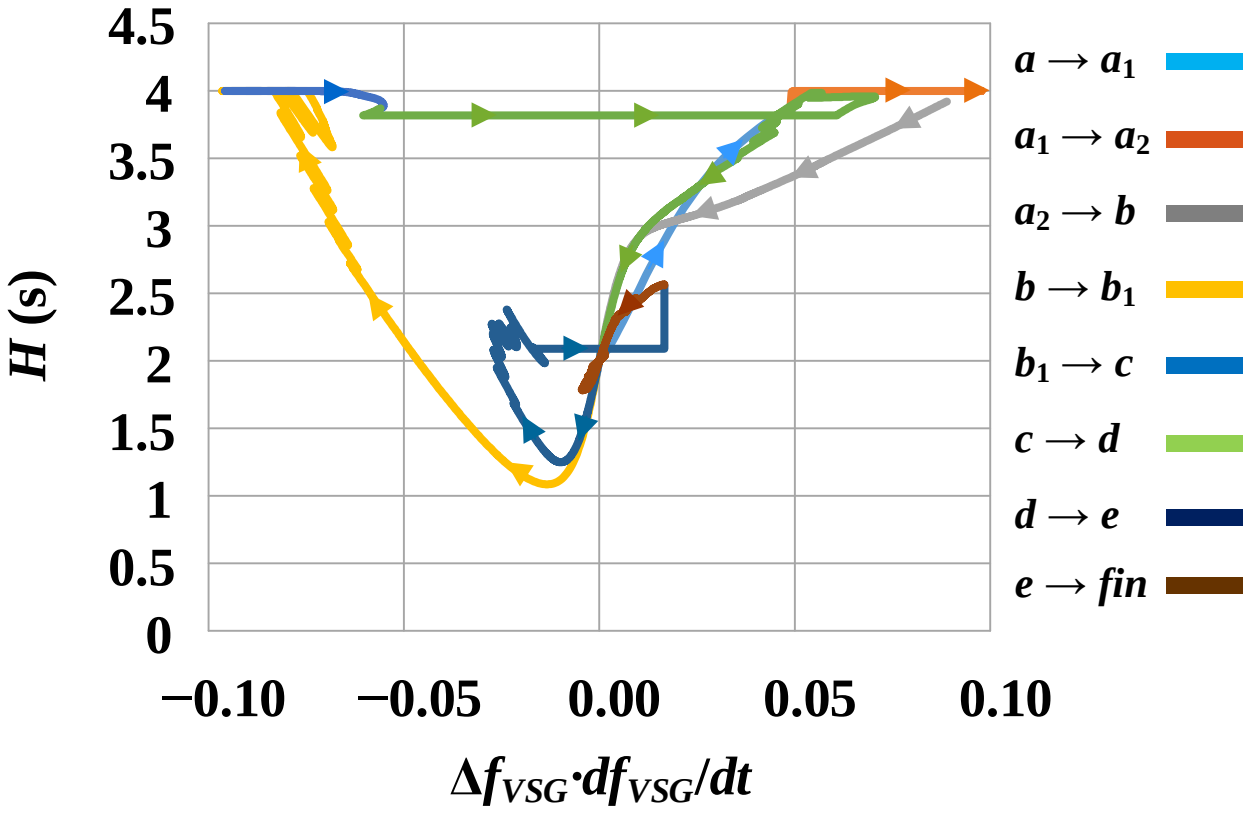

Figure 19. Behavior of virtual inertia under frequency changes.

Table 1. Operation stages of the proposed adaptive virtual inertia algorithm for the CC-VSG.

Stage	Δf_{VSG} Sign	df_{VSG}/dt Sign	df_{VSG}/dt < >$RoCoF_{set}$	k_{H1} Behavior	H_{VSG} Behavior
$a \rightarrow a_1$	>0	>0	<RoCoF	$k_{H1}\uparrow > 1$ (curve 1) *	$H_{VSG}\uparrow > H_0$ (curve 1) **
$a_1 \rightarrow a_2$	>0	>0	>RoCoF	k_{H1} = max (curve 1)	H_{VSG} = max (curve 1)
$a_2 \rightarrow b$	>0	>0	<RoCoF	$k_{H1}\downarrow > 1$ (curve 1)	$H_{VSG}\downarrow > H_0$ (curve 1)
$b \rightarrow b_1$	>0	<0	<RoCoF	$k_{H1}\downarrow < 0$ (curve 1)	$H_{VSG}\uparrow > H_0$ (curve 2)
$b_1 \rightarrow c$	>0	<0	>RoCoF	k_{H1} = min (curve 1)	H_{VSG} = max (curve 2)
c	<0	<0	>RoCoF	k_{H1} = max (curve 2)	H_{VSG} = max (curve 1)
$c \rightarrow d$	<0	<0	<RoCoF	$k_{H1}\downarrow > 1$ (curve 2)	$H_{VSG}\downarrow > H_0$ (curve 1)
$d \rightarrow e$	<0	>0	<RoCoF	$k_{H1}\downarrow < 0$ (curve 2)	$H_{VSG}\uparrow > H_0$ (curve 1)

* see Figure 13. ** see Figure 14.

The switching conditions between the selected pairs of coefficients A and B are determined based on the change in the damper winding virtual current, which is obtained according to (45), when (3) is given [43]:

$$i_{1q} = -\frac{1}{\omega_b R_{1q}} \cdot \frac{d\psi_{1q}}{dt} = -\frac{\tau_{1q}}{L_{1q}} \cdot \frac{d\psi_{1q}}{dt} \quad (45)$$

The use of the damper winding virtual current allows to control the CIG response throughout the transient, because this current is non-zero only during the transients. However, in order to implement the correct change of τ_{1q} and L_{1q} at different transient stages, it is also necessary to control the sign of the VSG frequency change Δf_{VSG}. The latter is explained by the transient oscillograms shown in Figure 20. In the normal steady-state conditions (range I in Figure 20), when $\Delta f_{VSG} = i_{1q} = 0$, the coefficients A and B in (31) and (32) are equal to their initial values ($A = 3$ and $B = 3$). In the case of a disturbance, when the VSG frequency increases $\Delta f_{VSG} > 0$ (curve 1), at the initial stage of the transient process (range II) there is first a sharp increase in the damper winding virtual current and then it decreases to zero, with $i_{1q} < 0$. On the contrary, when $\Delta f_{VSG} < 0$ after a disturbance (curve 2), the opposite situation is observed—$i_{1q} > 0$. Thus, by controlling only one of the parameters, it is not possible to provide adequate switching conditions between the pairs of coefficients A and B. The latter is determined by the fact that in both cases, either at decreasing or increasing frequency, it is necessary to reduce the response speed of the system and thereby reduce the RoCoF value by switching to the coefficients $A = 25$ and $B = 9$. At the next stage of the transient process (range III), during the sign change of current i_{1q}, it becomes possible to switch to another pair of coefficients, $A = 4$ and $B = 4$, in order to reduce the magnitude of frequency deviation and to further fast frequency recovery.

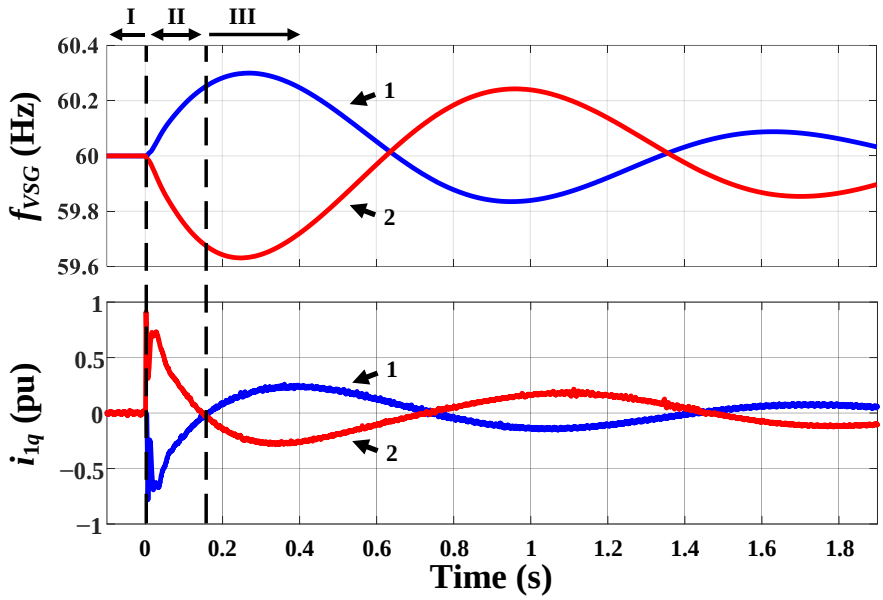

Figure 20. Oscillograms of damper winding virtual current under disturbances.

Consequently, the algorithm for changing the values of coefficients A and B and, accordingly, the parameters of the virtual damper winding τ_{1q} and L_{1q} is as follows (46):

$$[A \quad B] = \begin{cases} \begin{bmatrix} 25 & 9 \end{bmatrix} & \text{if } i_{1q} \cdot \Delta f_{VSG} < 0 \\ \begin{bmatrix} 3 & 3 \end{bmatrix} & \text{if } i_{1q} \cdot \Delta f_{VSG} = 0 \\ \begin{bmatrix} 4 & 4 \end{bmatrix} & \text{if } i_{1q} \cdot \Delta f_{VSG} > 0 \end{cases} \tag{46}$$

In summary, the operating principle of the proposed adaptive virtual damper winding algorithm is shown in Figure 21 for the case of grid frequency drop. As can be seen from the presented oscillograms, due to the implemented logic of the algorithm functioning, it becomes possible to significantly reduce both the RoCoF and the frequency nadir. At the same time, the frequency recovery rate together with the quality of damping remain at a high level.

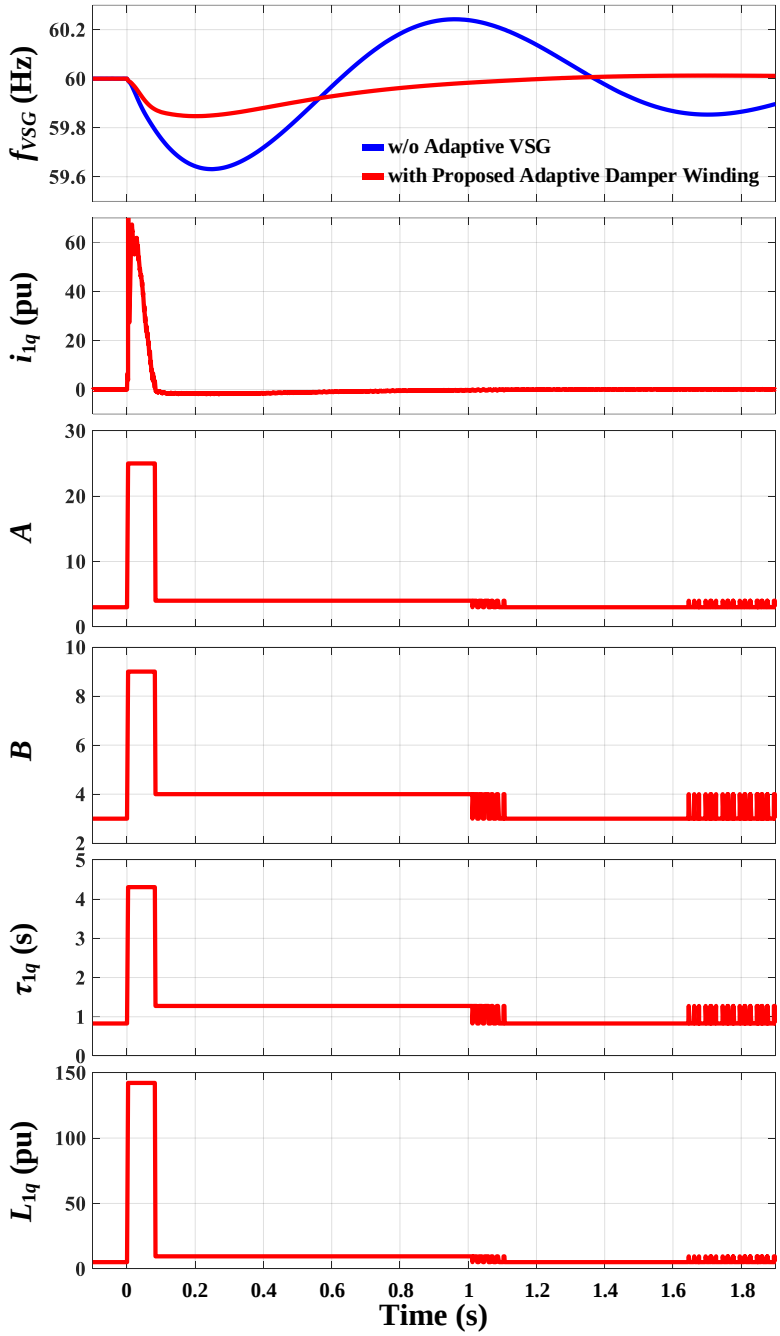

Figure 21. Operating principle of the adaptive virtual damper winding algorithm for the CC-VSG.

5. Simulation Results and Discussion

In order to assess the efficiency of the proposed CC-VSG control algorithm, a detailed time-domain mathematical modeling was performed in the equivalent scheme of the power system (Figure 1) via electromagnetic transient simulation tools. The parameters of the network, power converter and VSG-based control system are presented in Appendix A. The test disturbances were as follows: (1) a step change of P_{ref} from 0 to 0.2 pu, (2) a step grid frequency drop from 60 Hz to 59.9 Hz, and (3) a 0.5 MW load connection at the point of common coupling. Three cases were considered, as shown in Figure 22: CC-VSG without adaptive control (black curve), CC-VSG with adaptive virtual inertia only (blue curve), and CC-VSG with adaptive virtual inertia and damper winding (red curve).

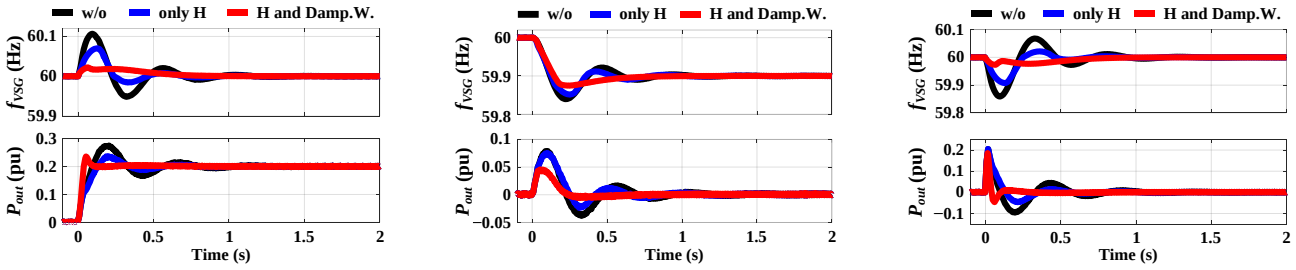

Figure 22. Simulation results under different disturbances: (**a**) change in P_{ref}, (**b**) grid frequency drop, and (**c**) load connection.

Based on the results obtained, it follows that by adding not only the adaptive inertia but also the adaptive damper winding to the CC-VSG control algorithm, it becomes possible to significantly improve the quality of damping without deteriorating the dynamic response under changes in the active power reference (Figure 22a). The latter is manifested in the maintaining and even improving of the rise time of the output power (Figure 23a). This proves the exclusion of the opposite mutual impact of the response speed of the active power control loop and oscillation damping capability.

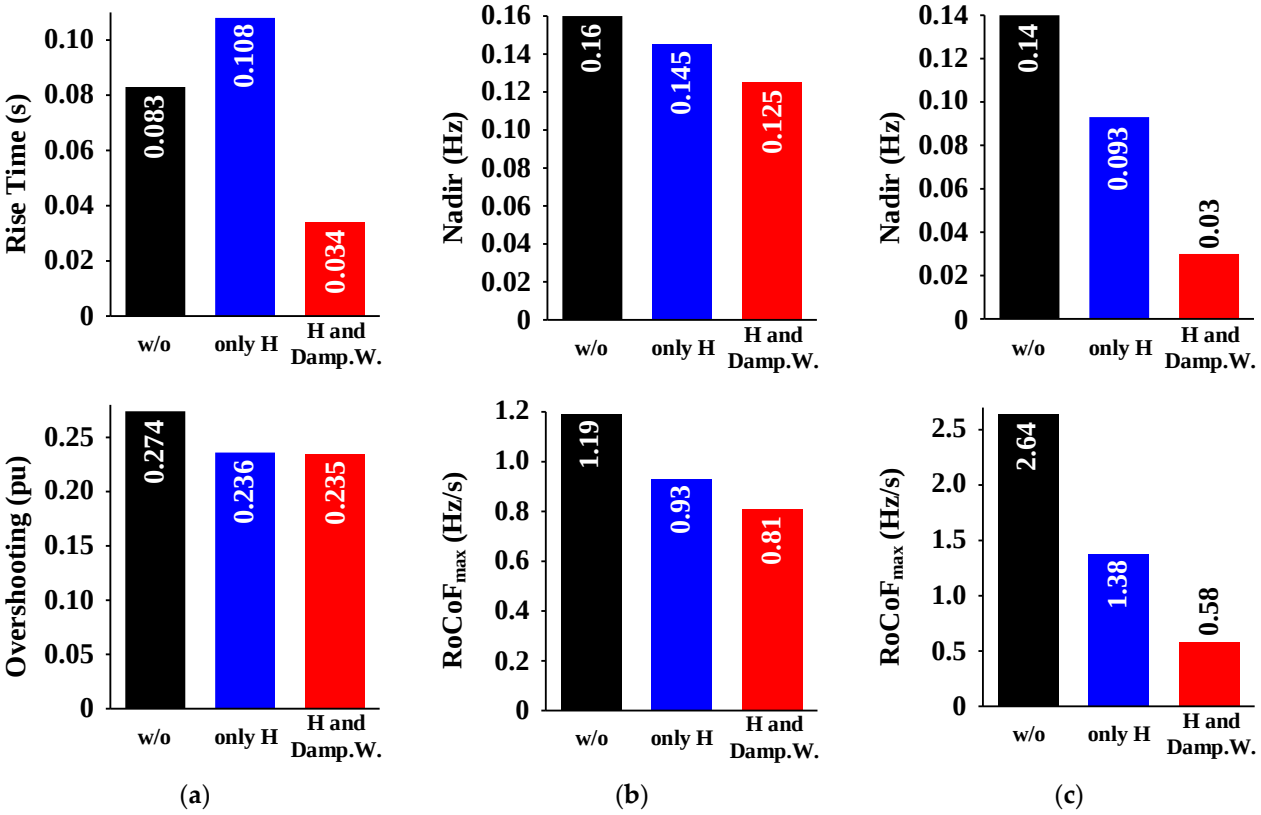

Figure 23. Histograms with transient characteristics under different disturbances: (**a**) change in P_{ref}, (**b**) grid frequency drop, and (**c**) load connection.

Considering the case with grid frequency change (Figure 22b), it can be seen that accounting of the adaptive damper winding in the proposed control algorithm allows to improve the frequency profile (Figure 23b). At the same time, there is no impact on the steady-state value of the output active power after the disturbance and, consequently, on the frequency droop. This conclusion confirms the leveling of the second contradiction arising from adding a damping coefficient to the swing equation of the VSG.

From the comparison of the results shown in Figure 22a,c, it follows that the proposed control algorithm of the CC-VSG helps to achieve a fast CIG response both in case of changes in the active power reference and in case of external disturbances, leading to frequency deviations. Thus, the introduction of the adaptive damper winding has no impact on the active power rise time, but it significantly improves the frequency profile. The latter is manifested in the reduction of RoCoF and frequency nadir by more than 4.5 times in comparison to the case without the adaptive CC-VSG (Figure 23c).

For assessing the efficiency of the proposed algorithm for the virtual inertia adaptive control based on the nonlinear sigmoid function, a similar 0.5 MW load connection at the point of common coupling at different settings of RoCoF was considered (Figure 24).

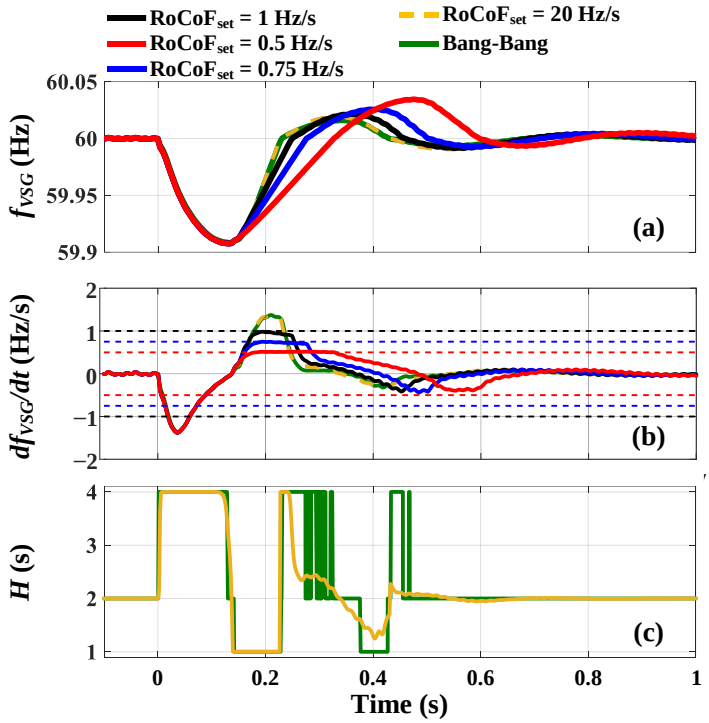

Figure 24. Resulting oscillograms under load connection and different RoCoF settings: (**a**) VSG frequency, (**b**) RoCoF and RoCoF$_{set}$, and (**c**) inertia of different control algorithms.

At the first step, the adaptive algorithm was compared with the conventional bang–bang control. For this purpose, the RoCoF$_{set}$ value was set to be large, as explained in Section 3 (RoCoF$_{set}$ = 20 Hz/s). The comparison of the green and yellow curves in Figure 24a,b shows that the proposed CC-VSG algorithm is nearly equal to the conventional bang–bang control, which is ensured by introducing an additional sensitivity index k_{H2} into (35). At the same time, based on the analysis of the change in the VSG inertia in Figure 24c, the proposed algorithm allows less DC-side energy consumption during the disturbance, which can be quantified by the area under the H_{VSG} curve [44]. As a result, the energy consumed using the proposed algorithm is ΔE = 4725, which is 21% less than the conventional bang–bang control with ΔE = 5973.

At the second step, the performance of the adaptive virtual inertia algorithm was assessed at different RoCoF settings. Considering the black, blue, and red curves in Figure 24a,b, it can be seen that the proposed algorithm allows to limit the RoCoF in accordance with the set references given the CIG capabilities, which are determined by the allowable range of the VSG inertia. However, at the initial stage of frequency change, the H_{VSG} range of a single CIG is insufficient to limit the RoCoF under the considered disturbance. In this case, it is necessary to increase the number of CIGs or the range of VSG inertia.

6. Conclusions

This paper proposes algorithms for adaptive control of virtual inertia and damper winding parameters for the enhanced structure of the current-controlled VSG. The results of analysis of the closed-loop transfer function for the active power control loop and simulation in the time domain proved that the proposed enhanced CC-VSG structure is devoid of three fundamental contradictions inherent in the conventional voltage-controlled VSG structure. Firstly, there is no opposite mutual impact between the response speed under the active power change and the oscillation damping capability. The addition of an adaptive algorithm for controlling the damping properties of the CC-VSG resulted in a significant reduction of the active power rise time under a disturbance of active power reference. Secondly, the introduction of the adaptive damper winding significantly improves the frequency profile—the RoCoF and frequency nadir or zenith are reduced. At the same time, there is no impact on the frequency droop. Finally, with an increase in the damping ratio, both the active power response and the output frequency response are improved simultaneously. Due to these properties, it was possible to achieve independent control of three parameters of the CC-VSG using the developed adaptive algorithms: virtual inertia, time constant, and inductance of the virtual damper winding. The use of nonlinear sigmoid function for adaptive control of virtual inertia allowed flexible control of the inertia value, according to the set RoCoF throughout the transient process. In addition, the proposed adaptive algorithm has reduced the DC-side energy consumption. Compared with the conventional bang–bang control, the reduction was 21%. At the same time, due to the additional sensitivity index, the proposed algorithm has a fast operation and high efficiency that are not inferior to the bang–bang control.

Author Contributions: A.S.: conceptualization, methodology, software, formal analysis, investigation, writing—original draft, writing—review and editing. A.A. (Alisher Askarov): conceptualization, methodology, investigation, writing—original draft, writing—review and editing. N.R.: conceptualization, software, writing—review and editing. V.R.: result analysis, resources, validation. P.R.: data curation, resources, visualization. A.A. (Andrey Achitaev): formal analysis, methodology. K.S.: supervision, writing—review and editing. All authors have read and agreed to the published version of the manuscript.

Funding: This study was supported by Russian Science Foundation, grant number 22-79-00204.

Data Availability Statement: No data were used for the research described in the article.

Conflicts of Interest: The authors declare no conflict of interest.

Appendix A

Table A1. Network and control system parameters.

Grid & Power Converter		CC-VSG		Adaptive Control	
Parameter	**Value**	**Parameter**	**Value**	**Parameter**	**Value**
V_b	480 V	H_0	2 s	$H_{\max}$	4 s
S_b	2 MVA	R_v	0 pu	$H_{\min}$	1 s
f_b	60 Hz	L_v	0.105 pu	a_H	1
f_{sw}	5 kHz	R_{1q}	0.01 pu	$\mathrm{RoCoF}_{\mathrm{set0}}$	0.5 Hz/s
L_f	0.1 pu	L_{1q}	0.71 pu	d_H	50
C_f	0.112 pu	K_u	1 pu	m_H	250
L_g	0.3 pu	$Q_{ref,VSG}$	0 pu	n_H	50
R_g	0 pu	K_{pcc}	0.052 pu		
		K_{icc}	13.195 pu		

References

1. Tan, B.; Zhao, J.; Netto, M.; Krishnan, V.; Terzija, V.; Zhang, Y. Power system inertia estimation: Review of methods and the impacts of converter-interfaced generations. *Int. J. Electr. Power Energy Syst.* **2022**, *134*, 107362. [CrossRef]
2. Rajan, R.; Fernandez, F.M.; Yang, Y. Primary frequency control techniques for large-scale PV-integrated power systems: A review. *Renew. Sust. Energ. Rev.* **2021**, *144*, 110998. [CrossRef]
3. Ilyushin, P.; Volnyi, V.; Suslov, K.; Filippov, S. Review of Methods for Addressing Challenging Issues in the Operation of Protection Devices in Microgrids with Voltages of up to 1 kV that Integrates Distributed Energy Resources. *Energies* **2022**, *15*, 9186. [CrossRef]
4. Craciun, B.I.; Kerekes, T.; Sera, D.; Teodorescu, R. Frequency support functions in large PV power plants with active power reserves. *IEEE J. Emerg. Sel. Top. Power Electron.* **2014**, *2*, 849–858. [CrossRef]
5. Cheng, Y.; Azizipanah-Abarghooee, R.; Azizi, S.; Ding, L.; Terzija, V. Smart frequency control in low inertia energy systems based on frequency response techniques: A review. *Appl. Energy* **2020**, *279*, 115798. [CrossRef]
6. Sosnina, E.; Dar'enkov, A.; Kurkin, A.; Lipuzhin, I.; Mamonov, A. Review of Efficiency Improvement Technologies of Wind Diesel Hybrid Systems for Decreasing Fuel Consumption. *Energies* **2023**, *16*, 184. [CrossRef]
7. Pourbeik, P.; Soni, S.; Gaikwad, A.; Chadliev, V. Providing primary frequency response from photovoltaic power Plants. In Proceedings of the CIGRE Symposium, Dublin, Ireland, 29 May–2 June 2017; pp. 1–10.
8. Ilyushin, P.; Filippov, S.; Kulikov, A.; Suslov, K.; Karamov, D. Intelligent Control of the Energy Storage System for Reliable Operation of Gas-Fired Reciprocating Engine Plants in Systems of Power Supply to Industrial Facilities. *Energies* **2022**, *15*, 6333. [CrossRef]
9. Rathnayake, D.B.; Akrami, M.; Phurailatpam, C.; Me, S.P.; Hadavi, S.; Jayasinghe, G.; Zabihi, S.; Bahrani, B. Grid Forming Inverter Modeling, Control, and Applications. *IEEE Access* **2021**, *9*, 114781–114807. [CrossRef]
10. Wang, X.; Taul, M.G.; Wu, H.; Liao, Y.; Blaabjerg, F.; Harnefors, L. Grid-Synchronization Stability of Converter-Based Resources—An Overview. *IEEE Open J. Ind. Appl.* **2020**, *1*, 115–134. [CrossRef]
11. Ilyushin, P.; Volnyi, V.; Suslov, K.; Filippov, S. State-of-the-Art Literature Review of Power Flow Control Methods for Low-Voltage AC and AC-DC Microgrids. *Energies* **2023**, *16*, 3153. [CrossRef]
12. Tamrakar, U.; Shrestha, D.; Maharjan, M.; Bhattarai, B.P.; Hansen, T.M.; Tonkoski, R. Virtual Inertia: Current Trends and Future Directions. *Appl. Sci.* **2017**, *7*, 654. [CrossRef]
13. Bevrani, H.; Ise, T.; Miura, Y. Virtual synchronous generators: A survey and new perspectives. *Int. J. Electr. Power Energy Syst.* **2014**, *54*, 244–254. [CrossRef]
14. Suvorov, A.; Askarov, A.; Kievets, A.; Rudnik, V. A comprehensive assessment of the state-of-the-art virtual synchronous generator models. *Electr. Power Syst. Res.* **2022**, *209*, 108054. [CrossRef]
15. Suvorov, A.; Askarov, A.; Bay, Y.; Maliuta, B.; Achitaev, A.; Suslov, K. Comparative small-signal stability analysis of voltage-controlled and enhanced current-controlled virtual synchronous generators under weak and stiff grid conditions. *Int. J. Electr. Power Energy Syst.* **2023**, *147*, 108891. [CrossRef]
16. Yang, X.; Li, H.; Jia, W.; Liu, Z.; Pan, Y.; Qian, F. Adaptive Virtual Synchronous Generator Based on Model Predictive Control with Improved Frequency Stability. *Energies* **2022**, *15*, 8385. [CrossRef]
17. Fu, S.; Sun, Y.; Liu, Z.; Hou, X.; Han, H.; Su, M. Power oscillation suppression in multi-VSG grid with adaptive virtual inertia. *Int. J. Electr. Power Energy Syst.* **2022**, *135*, 107472. [CrossRef]
18. Alipoor, J.; Miura, Y.; Ise, T. Power System Stabilization Using Virtual Synchronous Generator With Alternating Moment of Inertia. *IEEE J. Emerg. Sel. Top. Power Electron.* **2015**, *3*, 451–458. [CrossRef]
19. Li, J.; Wen, B.; Wang, H. Adaptive Virtual Inertia Control Strategy of VSG for Micro-Grid Based on Improved Bang-Bang Control Strategy. *IEEE Access* **2019**, *7*, 39509–39514. [CrossRef]
20. Malekpour, M.; Kiyoumarsi, A.; Gholipour, M. A hybrid adaptive virtual inertia controller for virtual synchronous generators. *Int. Trans. Electr. Energy Syst.* **2021**, *31*, e12913. [CrossRef]
21. Quint, R.; Ramasubramanian, D. Impacts of droop and deadband on generator performance and frequency control. In Proceedings of the 2017 IEEE Power & Energy Society General Meeting, Chicago, IL, USA, 16–20 July 2017; pp. 1–5.
22. Fang, H.; Yu, Z. Improved virtual synchronous generator control for frequency regulation with a coordinated self-adaptive method. *CSEE J. Power Energy Syst.* **2020**, 1–10. [CrossRef]
23. Zheng, T.; Chen, L.; Wang, R.; Li, C.; Mei, S. Adaptive Damping Control Strategy of Virtual Synchronous Generator for Frequency Oscillation Suppression. In Proceedings of the 12th IET International Conference on AC and DC Power Transmission (ACDC 2016), Beijing, China, 28–29 May 2016; pp. 1–5.
24. Shi, K.; Chen, C.; Sun, Y.; Xu, P.; Yang, Y.; Blaabjerg, F. Rotor inertia adaptive control and inertia matching strategy based on parallel virtual synchronous generators system. *IET Gener. Transm. Distrib.* **2020**, *14*, 1854–1861. [CrossRef]
25. Wang, Q.; Zhou, D.; Yin, S.; Lei, Y.; He, T. Improved Adaptive Inertia and Damping Coefficient Control Strategy of VSG Based on Optimal Damping Ratio. In Proceedings of the 2022 International Power Electronics Conference (IPEC-Himeji 2022-ECCE Asia), Himeji, Japan, 15–19 May 2022; pp. 102–107.
26. Qu, S.; Wang, Z. Cooperative Control Strategy of Virtual Synchronous Generator Based on Optimal Damping Ratio. *IEEE Access* **2021**, *9*, 709–719. [CrossRef]
27. Chen, J.; Liu, M.; Milano, F.; O'Donnell, T. Adaptive Virtual Synchronous Generator Considering Converter and Storage Capacity Limits. *CSEE J. Power Energy Syst.* **2022**, *8*, 580–590.

28. Li, M.; Huang, W.; Tai, N.; Yang, L.; Duan, D.; Ma, Z. A Dual-Adaptivity Inertia Control Strategy for Virtual Synchronous Generator. *IEEE Trans. Power Syst.* **2020**, *35*, 594–604. [CrossRef]
29. Sun, L.; Wang, P.; Han, J.; Wang, Y.; Yu, C.; Chen, M. Adaptive Inertia Control of Virtual Synchronous Generator Based on Power Feedback. In Proceedings of the 2021 IEEE 4th International Electrical and Energy Conference (CIEEC), Wuhan, China, 28–30 May 2021; pp. 1–5.
30. D'Arco, S.; Suul, J.A.; Fosso, O.B. A Virtual Synchronous Machine implementation for distributed control of power converters in SmartGrids. *Electr. Power Syst. Res.* **2015**, *122*, 180–197. [CrossRef]
31. Chen, M.; Zhou, D.; Blaabjerg, F. High penetration of inverter-based power sources with VSG control impact on electromechanical oscillation of power system. *Int. J. Electr. Power Energy Syst.* **2022**, *142*, 108370. [CrossRef]
32. Li, M.; Yu, P.; Hu, W.; Wang, Y.; Shu, S.; Zhang, Z.; Blaabjerg, F. Phase Feedforward Damping Control Method for Virtual Synchronous Generators. *IEEE Trans. Power Electr.* **2022**, *37*, 9790–9806. [CrossRef]
33. Chen, S.; Sun, Y.; Han, H.; Luo, Z.; Shi, G.; Yuan, L.; Guerrero, J.M. Active power oscillation suppression and dynamic performance improvement for multi-VSG grids based on consensus control via COI frequency. *Int. J. Electr. Power Energy Syst.* **2023**, *147*, 108796. [CrossRef]
34. Li, Y.; Fan, L.; Miao, Z. Stability Control for Wind in Weak Grids. *IEEE Trans. Sustain. Energy* **2019**, *10*, 2094–2103. [CrossRef]
35. Kundur, P. *Power System Stability and Control*; McGraw-Hill: New York, NY, USA, 1993.
36. Mandrile, F.; Carpaneto, E.; Bojoi, R. Grid-Feeding Inverter with Simplified Virtual Synchronous Compensator Providing Grid Services and Grid Support. *IEEE Trans. Ind. Appl.* **2021**, *57*, 559–569. [CrossRef]
37. Suvorov, A.; Askarov, A.; Bay, Y.; Ufa, R. Freely customized virtual generator model for grid-forming converter with hydrogen energy storage. *Int. J. Hydrog. Energy* **2022**, *47*, 34739–34761. [CrossRef]
38. Bissel, C. *A History of Automatic Control*; Springer: Berlin/Heidelberg, Germany, 2009; pp. 53–69.
39. Bissell, C. AA Andronov and the development of Soviet control engineering. *IEEE Control Syst. Mag.* **1998**, *18*, 56–62.
40. Wang, F.; Zhang, L.; Feng, X.; Guo, H. An Adaptive Control Strategy for Virtual Synchronous Generator. *IEEE Trans. Ind. Appl.* **2018**, *54*, 5124–5133. [CrossRef]
41. Li, D.; Zhu, Q.; Lin, S.; Bian, X.Y. A Self-Adaptive Inertia and Damping Combination Control of VSG to Support Frequency Stability. *IEEE Trans. Energy Conver* **2017**, *32*, 397–398. [CrossRef]
42. Fang, J.; Deng, H.; Goetz, S.M. Grid Impedance Estimation Through Grid-Forming Power Converters. *IEEE Trans. Power Electr.* **2021**, *36*, 2094–2104. [CrossRef]
43. Mandrile, F.; Carpaneto, E.; Bojoi, R. Virtual Synchronous Generator with Simplified Single-Axis Damper Winding. In Proceedings of the 2019 IEEE 28th International Symposium on Industrial Electronics (ISIE), Vancouver, BC, Canada, 12–14 June 2019; pp. 2123–2128.
44. Markovic, U.; Chu, Z.; Aristidou, P.; Hug, G. LQR-Based Adaptive Virtual Synchronous Machine for Power Systems With High Inverter Penetration. *IEEE Trans. Sustain. Energy* **2019**, *10*, 1501–1512. [CrossRef]